A Search for Type Ia Supernovae in Globular Clusters

Alan Howard Craggs

A thesis submitted in partial fulfilment

of the requirements for the degree of

Master of Science by Research

Jeremiah Horrocks Institute for Mathematics, Physics and Astronomy

University of Central Lancashire

June 2024

Declaration

Type of Award: Master of Science by Research

School: Engineering and Computing

I declare that while registered as a candidate for the research degree, I have not been a registered candidate or enrolled student for another award of the University or other academic or professional institution.

I declare that no material contained in the thesis has been used in any other submission for an academic award and is solely my own work.

No proof-reading service was used in the compilation of this thesis.

Alan Howard Craggs

June 2024

Abstract

In globular clusters the density is such that stellar interactions are commonplace. It is therefore expected that Type Ia supernovae explosions would occur within them at a high rate, however no Type Ia supernova has ever been observed in a globular cluster to date. We therefore carried out a search of records in the Open Supernova Catalog from the Zwicky Transient Facility (ZTF) survey to compile a list of Type Ia supernovae recorded there, with their respective coordinates, from 08/04/2018 to 20/11/2021. The survey has a limiting latitude value of $-27°$, which was in turn set as a limit for the project. A further limiting distance of 125 Mpc was also set, within which HyperLEDA extragalactic database was used to compile a sample of bright galaxies. A check was carried out to ensure both supernovae and galaxies were within the imposed limits with a final 307 supernovae and 56,903 galaxies and, using the Globular Cluster Luminosity Factor (GCLF) methodology from Jordán et al. (2007), a figure of 31,679 visible globular clusters was estimated. PanSTARRS and the Hubble Space Telescope (HST) imaging was used to view the supernova coordinates before and after the supernova event, with an image of the supernova also included from ZTF archives. No definite supernova was seen to occur in a globular cluster, but there were noted instances of correspondence between 3 supernovae and 3 potential Ultra Compact Dwarfs (UCDs) or compact Elliptical galaxies (cEs). The figures found from the project provided a supernova rate for the volume of $1.47 \times 10^{-5}\,\mathrm{yr}^{-1}\,\mathrm{Mpc}^{-3}$ and an upper limit on the globular cluster supernova rate of $2.52 \times 10^{-12}\,\mathrm{yr}^{-1}\,\mathrm{M}_{\odot}^{-1}$.

We feel that this is not yet a strong limit due to the small number of globular clusters surveyed, but are confident that it forms a sound basis for rapid increase in the following years using the Large Synoptic Survey Telescope (LSST).

Contents

Declaration ii

Abstract iii

Acknowledgements x

1 INTRODUCTION 1

1.1 Supernovae Fundamentals 1

1.2 Type Ia Supernovae 9

1.3 Globular Clusters (GCs) 15

1.4 Data Sources 22

1.4.1 The Zwicky Transient Facility (ZTF) 23

1.4.2 The Panoramic Survey Telescope and Rapid Response System (Pan-STARRS) 26

1.5 Data Use Methodology 28

2 DATA SEARCHES 29

2.1 Search for Supernovae 29

2.2 Search for Galaxies 30

2.3 Initial assessment and use of preliminary data 31

2.4 Statistical Basis of Globular Cluster Numbers 33

2.5 Cross-match of Supernova and Galaxy Lists 44

3 EXAMINATION OF COINCIDENCE **47**

3.1 Assessment of Areas of Interest 47

3.2 Examination of Three Coincidence Candidates 50

4 STATISTICAL ASSESSMENT OF RESULTS **57**

4.1 Consideration of Selected Volume 57

4.2 Total Stellar Mass Within the Volume 58

4.3 Consideration of Volumetric GC Mass Density 59

4.4 Consideration of Volumetric SNe Events 62

4.5 Consideration of Rate Limits 64

4.6 Concluding Summary 65

5 DISCUSSION **67**

5.1 Appreciation of Event Relationship 67

5.2 Future Research 69

6 CONCLUSIONS **71**

List of Tables

1 Table 3 from Peng et al. (2008), bin values for sample from Fig. 20 Above. 37

2 Comparative magnitude, luminosity and mass values. 55

3 Magnitude, luminosity and mass values of estimated GCs. 60

List of Figures

1 Fundamental supernova types. From Figure 1.9 of Dereli (2015) 2

2 Type II Supernova (SNII) basic lifecycle. Image credit: Brooks and Cole Thomson Learning. From www.astronomyonline.org. 3

3 Light curves of supernova types. From Figure 3 of Filippenko (1997) . . . 4

4 Type II spectra. Sourced from website www.astronomy.swin.edu.au. . . . 5

5 Type I spectra. Sourced from website www.astronomy.swin.edu.au. . . . 6

6 Roche Lobe and common envelope in Type Ia SNe, From Fig 1 of Ivanova et al. (2013) Labels: ZAMS - Zero Age Main Sequence; RLO - Roche Lobe Overflow; CE - Common Envelope; CO WD - Carbon-Oxygen White Dwarf; He - Helium. 9

7 Fundamental scenarios 13

8 Degenerate scenario results 14

9 Globular cluster M10 16

10 Population vs size relationship to core collapse of GCs. 17

11 Illustration of core collapse oscillations through binary-binary interactions and interspersed relaxation episodes. From Fregeau et al. (2003), Figure 5 19

12 Colour-Magnitude diagram showing evolutionary position of Blue Stragglers. From www.universetoday.com/wp-content/uploads/2008/12/m55cmd 21

13 Palomar Samuel Orchin 48” Schmidt telescope dome, California USA . . 23

14 ZTF Camera Installation 24

15 Pan-STARRS Facility on the Mountain of Haleakala, Maui 26
16 From Fig 3 Chambers et al. (2016) 27

17 Positions of full sample of target galaxies and SNe Type Ia 31
18 m_B to m_V relationship plot 32
19 Approximated scaling relationship between (logd25/2) and R_e 34
20 Figure 2 from Peng et al. (2008). Illustrating sample S_N - M_V relationship. 36
21 S_N - M_V relationship. Progressive assessments (top) Best fit choice (bottom)
Errors bars are from statistical S_N errors in sample bins from Peng et al. (2008) 38
22 Selection of generated Gaussian curves to illustrate the expected number of GCs visible. 42
23 Positions of final sample of target galaxies and SNe Type Ia 45

24 Selection of rejected image files 49
25 Candidate 1 51
26 Candidate 2 (red ring) 53
27 Candidate 3 (red ring) 54

28 Spherical sector volume graphic definition of terms. 57
29 Illustration of estimated GC masses for the remining 31,679 GCs 61

Acknowledgements

My sincere thanks are due to Dr. Mark Norris, who has shown incredible patience and support during the project, demonstrating his experience and enthusiasm in volumes only matched by those mentioned in this thesis. A mention also to Richard Pomeroy and Jason Kirk, for some detailed help on Python. Also, thanks goes to my long term contacts within UCLan and JHI, it doesn't seem like ten years since I started out on the DL Honours course, but I'm at this point now because of you all. Finally to my long suffering wife, Maureen who has put up with keyboard rage, long nights, anxiety (and me) throughout, thanks are due in droves - but I'm not finished yet I hope, because Astronomy has got me hooked.

We also acknowledge the use and importance of the following data repositories during the progress of this thesis:

The Open Supernova Catalog.

The HyperLeda database (http://leda.univ-lyon1.fr).

The Pan-STARRS1 data archive.

NASA's Astrophysics Data System.

The VizieR catalogue access tool (DOI : 10.26093/cds/vizier).

Chapter 1

INTRODUCTION

The aim of this Master's research project was to undertake a search for Type Ia supernovae (SNe) that have occurred in globular clusters (GC). Notwithstanding their high stellar density and high binary or tertiary system probability, to date no supernovae have been witnessed in a globular cluster. To better understand the subjects under scrutiny, some background introduction is provided in the following sections.

1.1 Supernovae Fundamentals

All stars eventually exhaust their fuel supply and come to the end of their lives, some of those via a specific type of explosive supernova (SN) event dependent upon their mass. There are two fundamental types of SNe, Type II and Type I, which are further subdivided based on their spectra or light curves which provide illustrative descriptions of events involving stars of varying mass, composition, decay process and binarity. The subdivisions provide a definite differential in the supernova progenitor explosion worth introducing here, where Type Ia are caused by thermonuclear runaway and all others by core collapse. Further details of these events will be provided later in this section and a summary illustration is included at Figure 1 below.

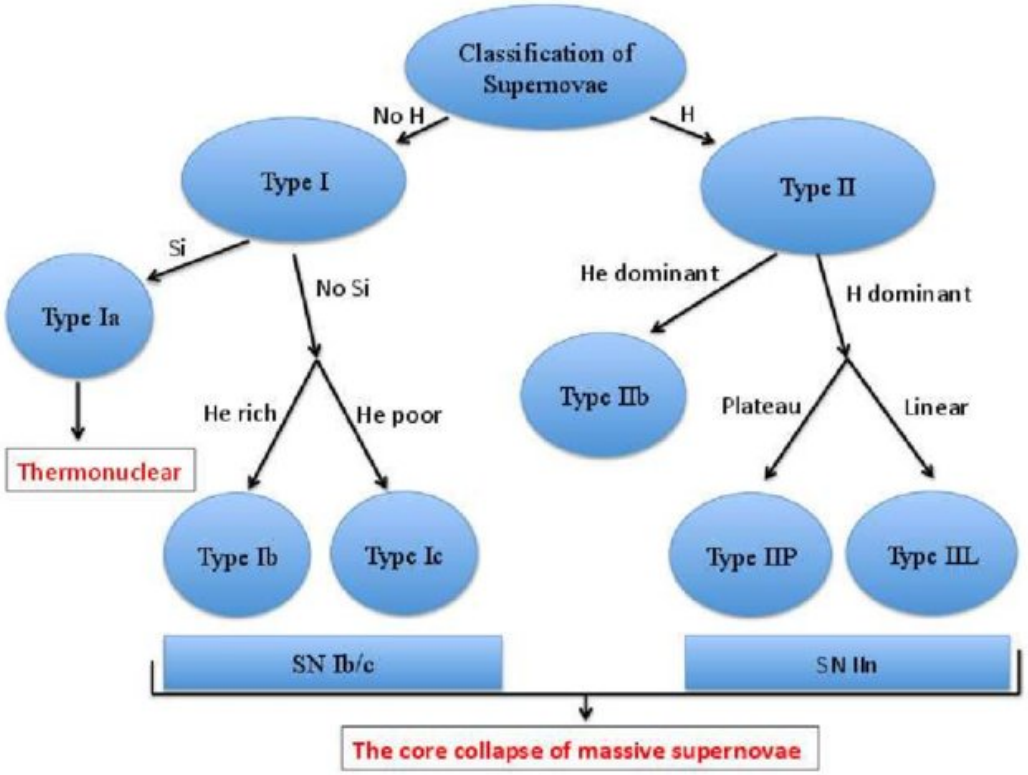

Figure 1: Fundamental supernova types. From Figure 1.9 of Dereli (2015)

Type II SNe occur in higher mass stars (8 $M_{\odot}$ < M_{orig} < 40 - 50 $M_{\odot}$) and are seen in spiral arms and H II regions of actively starforming galaxies. Their defining characteristic is the presence of hydrogen in their observed spectrum. They are generally not observed in elliptical galaxies because the stellar population of those galaxies typically comprise only of low mass stars ($M \lesssim 1M_{\odot}$) today due to their having ceased star formation several Gyr ago. The increased mass of the massive Type II SNe progenitors allows fusion of progressively heavier elements until a core of iron with nickel is formed, at which point no further energy can be extracted by fusion. As the mass of the inert core increases, eventually its own gravity exceeds the internal electron degeneracy pressure supporting the iron core, initiating a core collapse. This rapid collapse increases the pressure and temperature in the inner core, forcing protons and electrons together to form neutrons in a reverse beta-decay process. This newly created neutron core is held up by its own

degeneracy pressure, resisting further collapse and rebounding to create the conditions necessary to explode the outer layers of the star in a supernova event thereby ejecting the fusion products of the outer layers and the Hydrogen envelope.

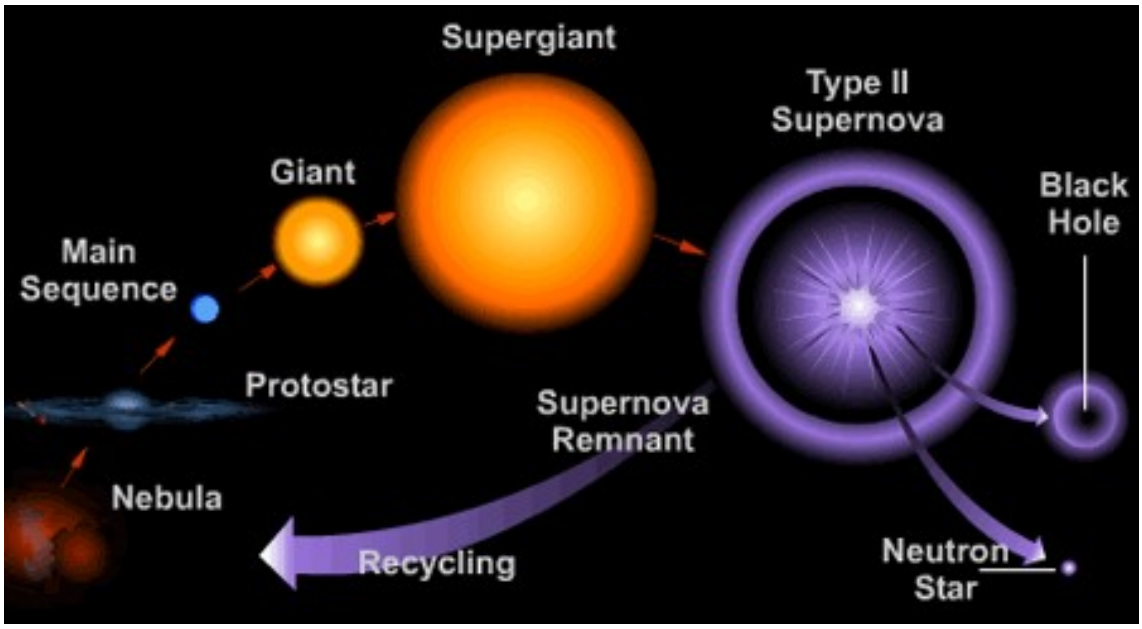

Figure 2: Type II Supernova (SNII) basic lifecycle. Image credit: Brooks and Cole Thomson Learning. From www.astronomyonline.org.

These elements are ejected into space with either a nebula of glowing gas remaining alone, or, dependent upon its original mass, it may contain either a neutron star (8 $M_{\odot}$ < M_{orig} < 20 - 25 $M_{\odot}$) (Lieb & Yau, 1987; Woosley et al., 1987; Heger et al., 2003; Fryer & New, 2011), or a black hole (20 - 25 $M_{\odot}$ < M_{orig} < 40 - 50 $M_{\odot}$) (Woosley et al., 1987; Fryer, 2003). Beyond that mass, the theory is that it collapses to a black hole without the SN explosion (Fryer, 1999; Woosley et al., 1987). See Figure 2 above for illustration of the basic Type II lifecycle showing differing results as noted.

The subdivisions for Type II are II-L, II-P, IIn and IIb. Types II-L and -P are based on their light curve decay, where -L (indicating a linear slope, even though it is not actually a straight line) have a steady progression after the brightest measurement, but -P (indicating a plateau in the slope) have a halt in their decay forming a flatter phase in the post-maximum curve before resuming the decline. See Figure 3 below.

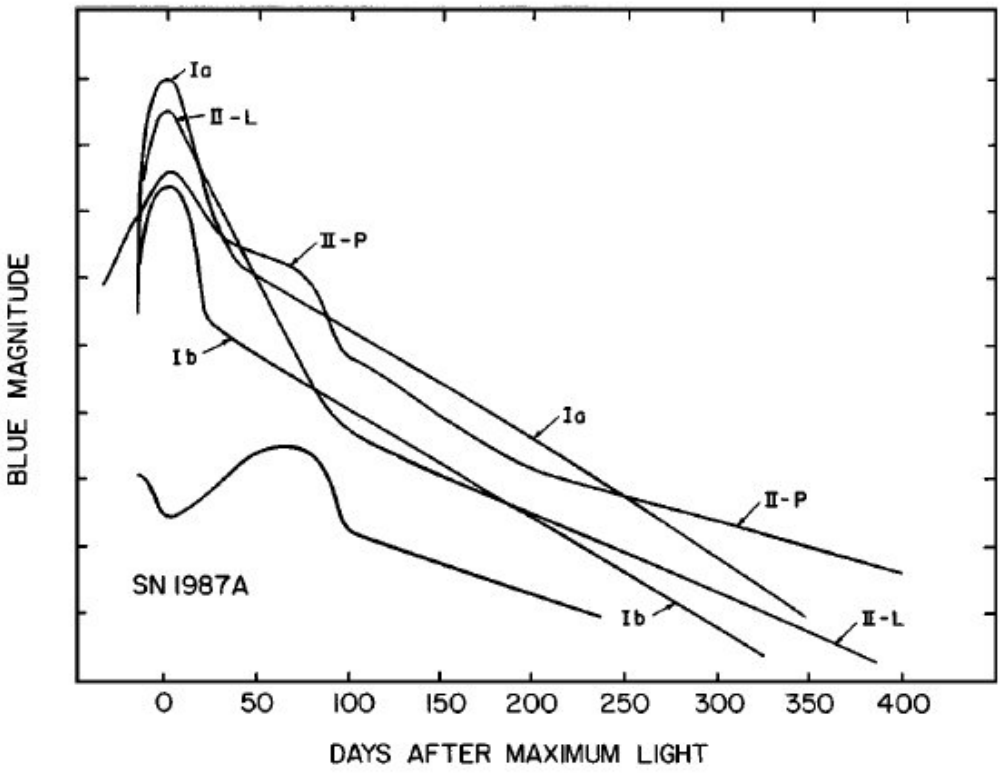

Figure 3: Light curves of supernova types. From Figure 3 of Filippenko (1997)

The reasons given for this are that the -L type explosion blows away the majority of the hydrogen in the progenitor, whereas the -P type explosion shock wave ionises the hydrogen, rather than wholesale expulsion in what is probably a more hydrogen-rich progenitor, maintaining a level of opacity and halting the linear decay until it cools and returns the light curve to the linear decay phase (Doggett & Branch, 1985; Nagy et al., 2014).

Types IIn and IIb are distinguished by their spectra, where ‘n’ in the description of IIn indicates a narrow hydrogen emission line typically at FWHM $\lesssim$ 200 km s^{-1} (Filippenko, 1997), whereas IIb SNe have a weak hydrogen emission line which disappears as the light curve decays to leave a curve which resembles a Type Ib SN similar to that curve labelled SN 1987 A in Figure 3 above, hence the ‘b’, where the similarity to the Type Ib curve can be seen in Figure 5 below (Woosley et al., 1987; Arnett & Fu, 1989; Patat et al., 1994; Filippenko, 1997; Hillier & Dessart, 2019).

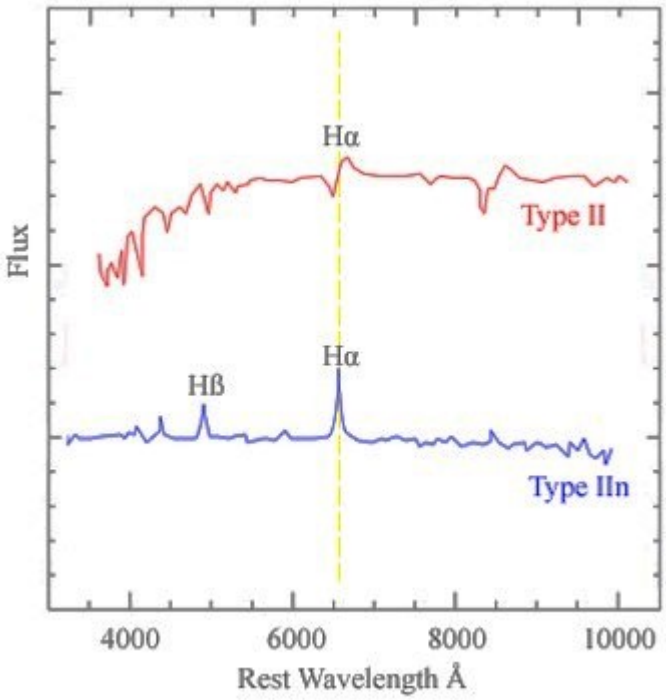

Figure 4: Type II spectra. Sourced from website www.astronomy.swin.edu.au.

It was initially theorised that Type I SNe also occur due to a star losing its outer layers and succumbing to core collapse, as for Type II SN. However, as introduced above, it is now believed that of the Type I subtypes, Type Ia SNe result from binary evolution leading to a white dwarf undergoing a catastrophic runaway fusion reaction, where the other Type I subtypes undergo core collapse as their Type II counterparts, see Figure 1. This will be discussed in more detail in Type Ia Section 1.2 below.

The subdivisions for Type I are Ia, Iax, Ib and Ic, where types Ib and Ic are categorised by aspects of their spectra, where no absorption line of singly ionized silicon at λ = 635.5 nm exists (da Silva, 1993; Filippenko, 1997). Types Ib and Ic also include lines of oxygen, calcium and magnesium as they age, where Type Ia display an absence of hydrogen and helium, signs of nuclear processing of silicon, sulphur and calcium, but notably an eventual dominance of iron.

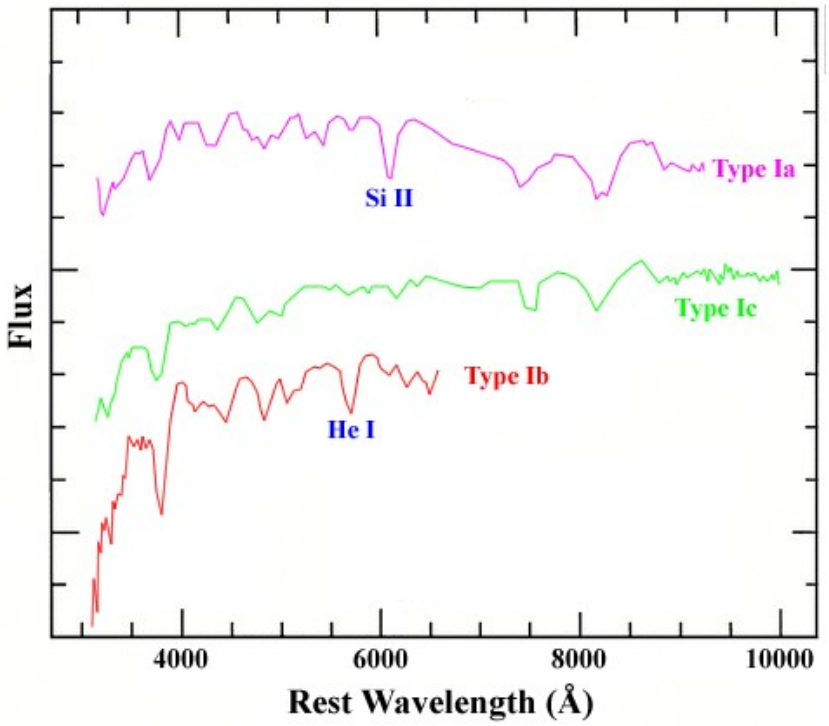

Figure 5: Type I spectra. Sourced from website www.astronomy.swin.edu.au.

The difference between Ib and Ic SNe is that Ic have no helium lines at 587.6 nm (Branch & Wheeler, 2017). Type Ia and Iax however are seen in binary systems where the primary partner is more massive than the secondary and so evolves at a faster rate than the other, eventually becoming a white dwarf which leeches material from its binary system partner until it becomes massive enough to approach instability (see below), satisfying pre-explosion parameters.

In the case of a Type Ia, this results in a thermonuclear SN explosion through deflagration (Baron et al., 1987; Lieb & Yau, 1987; Fryer & New, 2003). However, Type Iax results from a carbon - oxygen white dwarf accreting helium from a He companion until it nears the instability mass (see below), which initiates a deflagration propagation with surface explosions, while not necessarily completely disrupting the star (Foley et al., 2013; Jha, 2017).

Also worth an introduction here is cataclysmic variables. These are binaries that have a smaller mass WD as the primary partner and the accretion of material from the donor star increases temperature and pressure to the extent that a surface runaway hydrogen fusion occurs and much of the already accreted material is blasted into space in a dwarf nova. The accretion process begins again and this can lead to differing conclusions. As the stars lose material in a succession of dwarf novae, the donor will evolve also to a WD concluding with a merger and, due to the expected low mass of the two, the resultant single WD will progress to it's cooling phase without further action. However, there may be occasions where the material gathered by the primary member WD, or the resultant WD mass subsequent to the merger, pushes it toward the Chandrasekhar limit to produce a Type Ia SN (Warner, 2003; Walder et al., 2010).

With regard to the cosmological importance of SNe, these events share out the elements produced during the nuclear processes in their latter stages of life, along with those heavier and more precious which are subsequently formed in the final explosion, providing chemical enrichment in the next evolutionary step of the universe. We also see that the sheer energy wavefront of the outbursts may compress and excite the molecular clouds of gas and dust in the host galaxy into star formation, as well as ejecting and depositing material in the outer reaches. We know galactic star formation is initiated and sustained by gas accreted from the surrounding medium in the galaxies and from those regions where the SNe have supplemented its volume, which provides us with another SN driven evolutionary activity. Where infall of this gas has been observed, some of it is thought

to be undergoing recycling, after being initially enriched and ejected by SN events in the early universe, which provide a progressive heavy element content as the galaxy evolves as pointed out in the Editor's summary of Zhang et al. (2023).

As this project specifically targets Type Ia SNe, further detail will be presented in subsequent sections for those events alone, as they are the predominant SN type found in old stellar populations such as GCs today, as in such systems stars more massive than $8M_{\odot}$ have long since died.

1.2 Type Ia Supernovae

Type Ia SNe occur in evolved binary systems where a pair of stars both less massive than $8M_{\odot}$, initially on the main sequence and due to the evolutionary timeline are population II stars, form a tight binary system. The more massive of the stars, the primary partner, will have evolved to form a white dwarf, whilst the secondary will reach the expanded red giant phase when its ejected outer material cloud will be large enough to fill and exceed its Roche Lobe to begin mass transfer, sometimes covering both partners in what is termed a common envelope, illustrated in Figure 6 below.

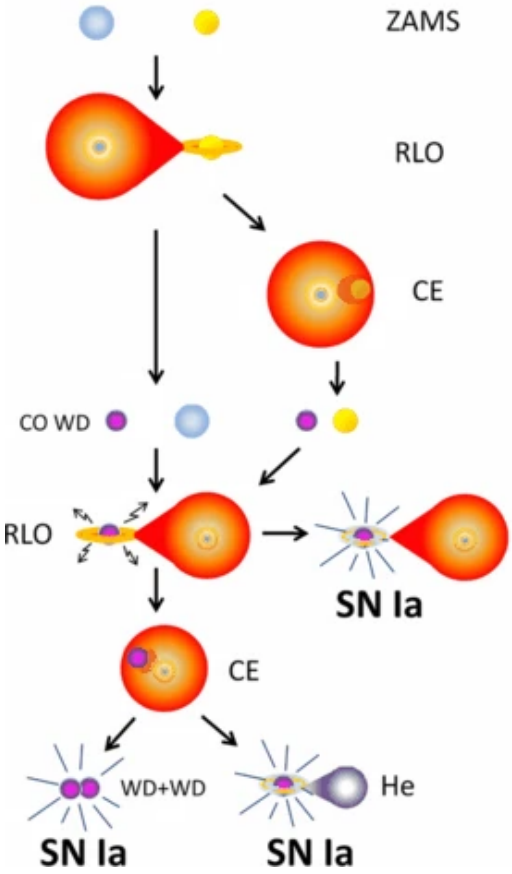

Figure 6: Roche Lobe and common envelope in Type Ia SNe, From Fig 1 of Ivanova et al. (2013) Labels: ZAMS - Zero Age Main Sequence; RLO - Roche Lobe Overflow; CE - Common Envelope; CO WD - Carbon-Oxygen White Dwarf; He - Helium.

In way of explanation of the terms used in describing the binary systems and of the elements shown in Figure 6, the Roche Lobe is the tear-shaped volume around the donor star which is filled with it's ejected outer layers of material. Whilst the material remains gravitationally bound to the donor, the boundaries of the lobe are maintained, with the 'sharp' portion of the lobe seen to be attracted toward the primary white dwarf. As the donor star's material continues to be ejected, the gravitational equilibrium of the lobe is compromised, the boundaries are breached and the now unconstrained material from the donor star is progressively gravitationally transferred to the primary member either in a direct stream or within a common envelope of the donor star's material. Common envelopes were postulated in the 70s to be an element of the lifecycle of binary system development, where a range of products were thought to be left by the interaction of the binary partners, namely merged white dwarfs, neutron stars or black holes, sometimes in pairs and also Type Ia SNe. The material from the donor star continues transference to the primary member within the envelope and, dependent upon the proximity of the binary partners along with the period and eccentricity of the orbit, the system will eject the majority if not all of the envelope. The alternative product, where the envelope is not ejected, sees the pair merge. (Paczynski, 1976; Podsiadlowski et al., 2002; Izzard et al., 2012; Ivanova et al., 2013; Li et al., 2022).

Due to the material transfer, the mass of the white dwarf is progressively increased toward instability. However, rather than the collapse of the primary's core after passing the Chandrasekhar limit of 1.44 $M_{\odot}$ being causative to the Type Ia SN explosion, the reasoning now is that the core temperature is raised due to its increasing density and pressure as the limit is approached (Mazzali et al., 2007). Subsequent to attaining a figure in the region of 99% of the Chandrasekhar limit (Wheeler et al., 1998), a period of about one thousand years of convection is entered (Hillebrandt & Niemeyer, 2000). During this period, the increasing temperature reaches a value that sees carbon fusion reoccur in the core, which causes the ignition of a deflagration flame front or fronts at some point or

points (Science Summary, 2004). How the proportion of carbon to oxygen in the core would affect the peak luminosity value of the SN, as oxygen fusion occurs shortly after the carbon reaction, is also under investigation (Röpke & Hillebrandt, 2004).

As there is no scope for a white dwarf to control its temperature via expansive cooling due to the degenerate state of the matter, the reactions begin to run away and the SN ignites through some, as yet unproven, initiation process (Hillebrandt & Niemeyer, 2000; Gamezo et al., 2003; Starrfield et al., 2016). The fusion of the carbon and oxygen continues to form heavier elements in the outer regions of the star, but in the inner regions higher mass nickel is synthesised within an extremely short timescale (Röpke & Hillebrandt, 2004). The associated fusion energy released, in a range of between 1 and 2×10^{44} J within just a few seconds, heats the white dwarf body to billions of degrees (Khokhlov et al., 1993), producing sufficient energy to unbind the star's material. This results in an extremely powerful explosion, with the ejecta on the shock wave travelling at speeds of between 5,000 and 20,000 kms^{-1} and being heated as it expands by the release of decay energy from nickel (^{56}Ni) through cobalt (^{56}Co) and onto iron (^{56}Fe). This event blasts every part of the white dwarf into space, leaving behind no compact remnant, only a diffusing envelope of gas.

During the expansion and heating phase of the explosion, the photosphere in turn moves through the hot regions of the ejecta and as the remains of the star dissipate and thin out, the light can be observed until it decays away to its lower value as an expanding gas shell remnant, as noted above. The brightening of the SN lightcurve to a large peak of absolute v-band magnitude of $M_V \approx$ -19.3 is directly driven by the energy released during the decay of the nickel (half-life ($t\frac{1}{2}$) of 6.077 days), which is taken over by the decay of cobalt (half-life ($t\frac{1}{2}$) of 77.236 days) as the brightness recedes (Pagel, 1997; Mazzali et al., 2007). This peak value is seen to be reached after a period of $\approx$ 15 to 20 days, whereafter it dims by around 3 mag in the first month after peak followed by a dimming of around 1 mag per month until no longer visible (Hillebrandt & Niemeyer, 2000).

There are three Type Ia progenitor suggestions. Within the common envelope, the secondary partner may in some circumstances be: firstly, another type of star; secondly, another, lesser mass white dwarf or lastly, the remaining carbon – oxygen core of an asymptotic giant star.

The first of the above suggestions, with a single white dwarf in the pair, is classified as a single-degenerate scenario (Nomoto, 1982; Canal et al., 1996). In this case, within the common envelope, material is accreted onto the white dwarf (see Figure 7 below) until the Chandrasekhar limit is approached, i.e. 1.39 – 1.44 $M_{\odot}$ dependent on chemical composition of the star (as the limit is derived from element specific degeneracy pressure), when it becomes unstable and satisfies the deflagration parameters based on the mass of the white dwarf and the accretion rate, resulting in one of two primary events. One being the initiation of a runaway thermonuclear reaction as the white dwarf approaches the Chandrasekhar mass limit, resulting in a SN explosion which ejects around a solar mass of heavy elements up to and including iron into space. The white dwarf mass, accretion rate and hydrogen or helium companion parameters have a bearing on the type of explosion in this event, seeing multiple flashes, delayed explosion and varying strengths of hydrogen or helium winds which affect the companion's envelope as the varying results (Nomoto & Leung, 2018). The other, extremely rare, event is due to a slower, asymmetric rather than central ignition and burning process, classified off-centre, leading to a massive compression event without total ejection, leaving behind a neutron star as the right frame in Figure 8 (Lieb & Yau, 1987; Canal & Gutiérrez, 1997; Nomoto & Leung, 2018).

The second, with a pair of white dwarfs, is classified as a double-degenerate scenario, where the white dwarfs lose angular momentum as they orbit one another until they merge (see Figure 7 below). If the combined mass of the resultant merger does not exceed Chandrasekhar limit, then the remaining, newly merged, dwarf proceeds along its normal lifecycle. If the primary gains enough mass to approach the Chandrasekhar limit, then the result is a SN explosion as above and as the left frame in Figure 8 (Schwab et al., 2016).

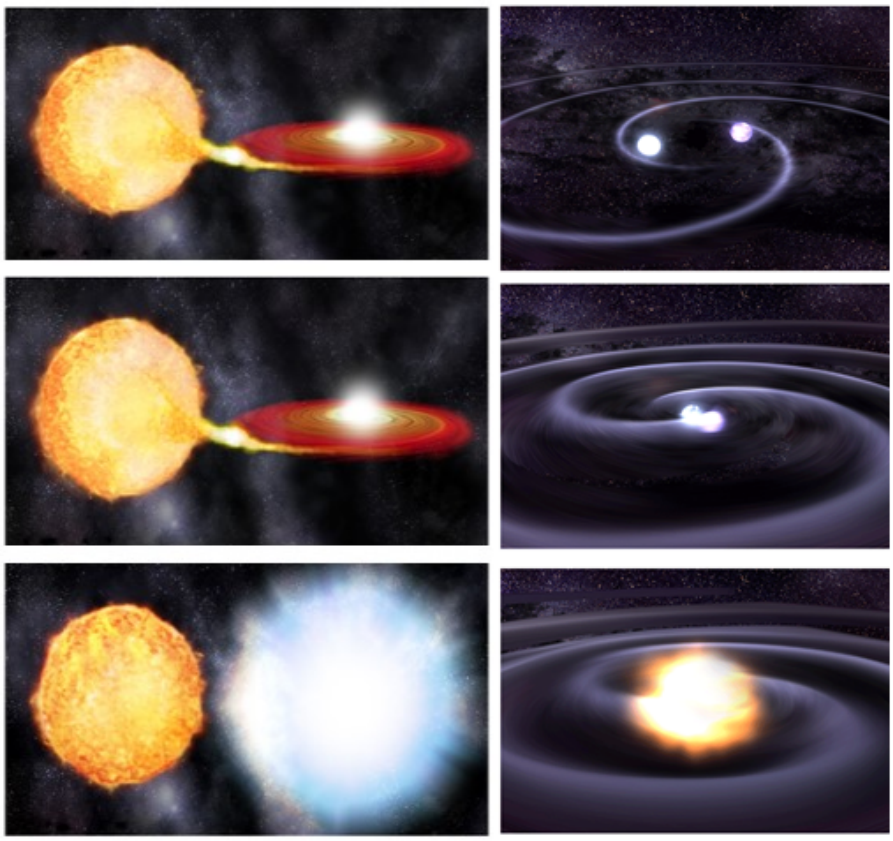

Figure 7: Fundamental scenarios

Single-Degenerate (L) and sub-chandrasekhar limit double-degenerate (R), see also Figure 8 below From, www.astrobites.org/wp-content/uploads/2015/04/two sne.png

The resultant Type Ia SNe explosions from either of the first two scenarios occur with the same pattern and therefore present predictable and consistent observational parameters, as 'standard candles', where distances can be measured using the accepted, and very bright, maximum absolute magnitude v-band figure of $M_V \approx$ -19.3 (Hillebrandt & Niemeyer, 2000). However, the suggested double degenerate scenario has provided some discussion regarding the constancy of all Type Ia SNe. It is thought that the double-degenerate merger of differing mass companions could perhaps produce some new white dwarfs able to exceed the Chandrasekhar limit, which in turn would possibly result in explosions of differing luminosity (Voss & Nelemans, 2012; Schwab et al., 2016).

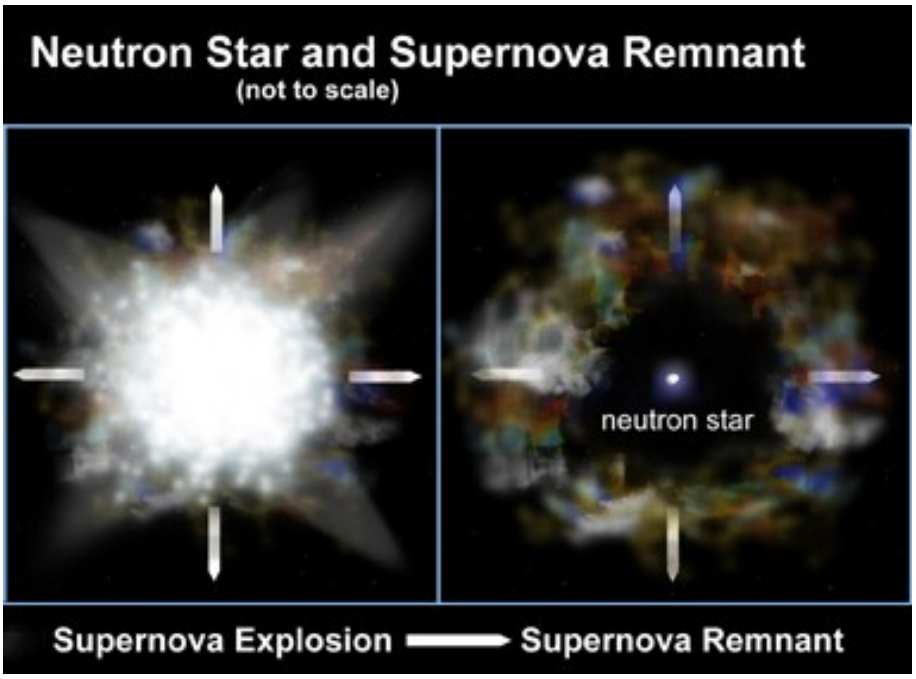

Figure 8: Degenerate scenario results

SN explosion and rare neutron star remnant Credit: NASA/Chandra X-ray Center/Penn State University. From, www.nasa.gov/missions/science/f supernovae.html

Nonetheless, at present, the brightness of the Type Ia SNe and their accepted high level of consistency sees their continued use as standard candles where they make excellent probes of cosmology. As an illustration, when observed, the SNe are fainter than expected at the given redshift indicating some extra expansion of the universe. Research in this field is important in the examination of dark energy and its effects in that expansion, helping to probe fundamental properties of the universe (Riess et al., 1998; Perlmutter et al., 1999; Perlmutter & Schmidt, 2003).

The third progenitor suggestion, of a white dwarf and an Asymptotic Giant Branch (AGB) core, is classified as a core-degenerate scenario, a rare SN progenitor that avoids off-centre ignition and proceeds to the SN explosion via the loss of angular momentum of a merger resultant, rapidly rotating massive white dwarf, causing its collapse (Soker, 2011; Zhou et al., 2015).

1.3 Globular Clusters (GCs)

Collections of stars are categorised from small open clusters to massive galaxies with several subcategories, including GCs, which comprise of a dense, near symmetrically spheroidal, gravitationally self-bound group of stars where no dark matter component is required. There are large numbers of GCs in the haloes of some galaxies and over 150 in the Milky Way, but the most massive galaxies host GC populations well in excess of 10,000 (Jordán et al., 2004; Tamura et al., 2009).

There is a classification system for GCs put in place by Harlow Shapley and Helen Sawyer Hogg (the Shapley-Sawyer Concentration Class, 1929) based on the stellar concentration toward the core of the GCs, with Class I having the highest concentration and Class XII the least (Sawyer Hogg, 1965). However, as investigation into GC evolution is progressing, varying classification parameters are being proposed regularly based on chemical evolution, mass and age, spectroscopy and photometry. That detail is not currently a primary influence in this project, but may become so in further investigation of the subject (Gratton et al. 2019 and references therein).

GCs were mistaken for stars in the early days of astronomy, but they were eventually included in Messier's catalogue of nebulae and star clusters when the improved optical instruments of the 1700s found that they were in fact clusters of many individual stars. They can number from tens of thousands to perhaps up to ten million members with cluster masses from 10^4 – 10^7 $M_\odot$. They typically have half mass radii of between three and five pc across but a handful of the largest may reach over 90 pc, with the stellar density increasing from the edges inward to the centre of the cluster where the densities can reach toward $1000\,M_\odot\,pc^{-3}$ (Marx & Pfau, 1992). At a mean absolute magnitude of around a figure of Mv = -7.5 mag (Jordán et al., 2007), with the brightest generally being up to Mv ~ -13 (Norris & Kannappan, 2011; Norris et al., 2014, 2019), (although some may be brighter) they are bright, but they also typically comprise ancient Population II, metal poor stars that are usually 8 - 10 billion years old (Gratton et al., 2019; Beasley, 2020),

however there are instances of multiple population GCs (Ziliotto et al., 2023) and also of SNe enrichment (Lee et al., 2009), illustrating some diversity in GC evolution although not yet fully explained.

Figure 9: Globular cluster M10

Illustrative example of a globular cluster, M10 in Ophiuchus, which is a Type VII GC approximately 4.5 pc distant. Left: In-field image of M10. Right: Image of M10 Core Images credit: Left: Credner, Kohle (Bonn University), Hoher List Observatory. Right: ESA and Hubble/NASA

Considering the high stellar density environment in GCs, it might be expected that the frequency of tight binary/tertiary systems is higher than in galactic field populations due to more frequent stellar interactions (Bahramian et al., 2013). Field stars average around 41%±2% growing to 53%±20% for low metallicity stars (Yuan et al., 2015), but the binary fraction in GCs is more difficult to assess due to the uncertainty surrounding the exact process of their evolution. The present thinking is that the GCs, although densely gravitationally bound, have weak binding energy and escape velocities are easily achieved allowing tidal disruption to occur either from external or host galaxy gravitational effects, or internal binary energy and gas loss effects.

Within the GCs, however, size and population combinations affect evolution, which can be a collapse of the GC core or, alternatively, a requisite amount of binary heating energy at the core that halts the collapse in favour of expansion to tidal disruption. The related parameters considered in the alternatives are the size of the GC, based on its virial radius, along with its stellar population, considered as the minimum value, which determines whether the GC will tidally disrupt before undergoing core collapse. As an example which provides expected GC density at galactic positions, O'Leary et al. (2014) provides an illustration in explaining that at the solar galactocentric radius of $R_G = 8.5$ kpc, a GC would be expected to have $\gtrsim 300$ stars and would more likely undergo tidal disruption than core collapse (see below Figure 10).

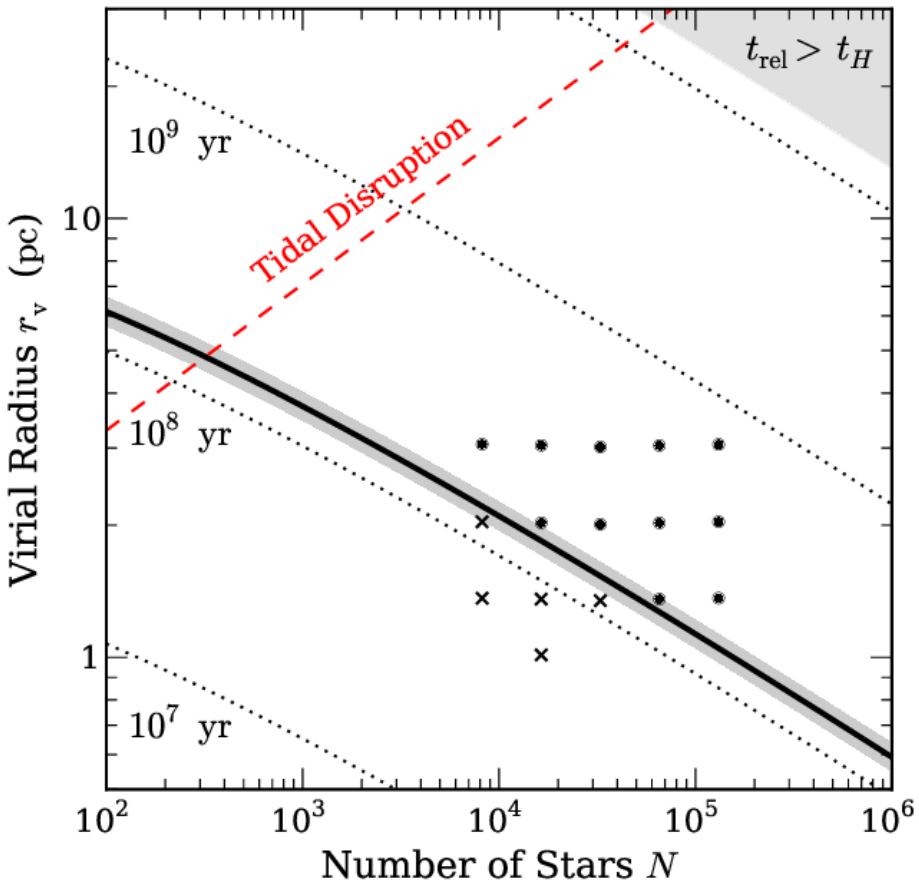

Figure 10: Population vs size relationship to core collapse of GCs.

From O'Leary et al. (2014), Figure 1

Pertinent explanatory text from O'Leary Figure 1.: 'The collapse line in the $r_v - N$ plane. Clusters starting above the solid curve undergo core collapse if they survive long enough. Those starting below the curve never experience core collapse. Finally, clusters starting above the diagonal, dashed line are tidally disrupted at a Galactocentric distance of 8.5 kpc. Each dotted, diagonal line represents the relaxation time t_{rel}. Clusters in the upper, shaded region have relaxation times greater than t_H, the Hubble Time, and so never relax. The shading around the solid curve shows the range of values it may take depending on the cluster's precise initial conditions. (Referencing O'Leary's simulations) the crosses represent clusters that failed to achieve core collapse, while filled circles are clusters whose central number density eventually increased.'

The core collapse scenario, which increases the stellar density in the central regions of the GC, sees more interactions, providing an enhancement of tight binary systems. Theories now say that after collapse, the consequential increase of interactions initiates binary burning to counteract the collapse until that energy is used and compression begins again, leading to a cyclic series of compression/relaxation episodes as shown in Figure 11 below taken from Figure 5 of Fregeau et al. (2003). This figure is based on using a model with $N = 3 \times 10^5$ stars with a 20% figure of primordial binaries. It is used here to better illustrate the compression/relaxation phases (Fregeau et al., 2003; Pooley, 2010; O'Leary et al., 2014; Pooley, 2016). Should any further detail on relaxation be required, it can be found in Baumgardt (2017); Hénault-Brunet et al. (2019); Meiron & Kocsis (2019).

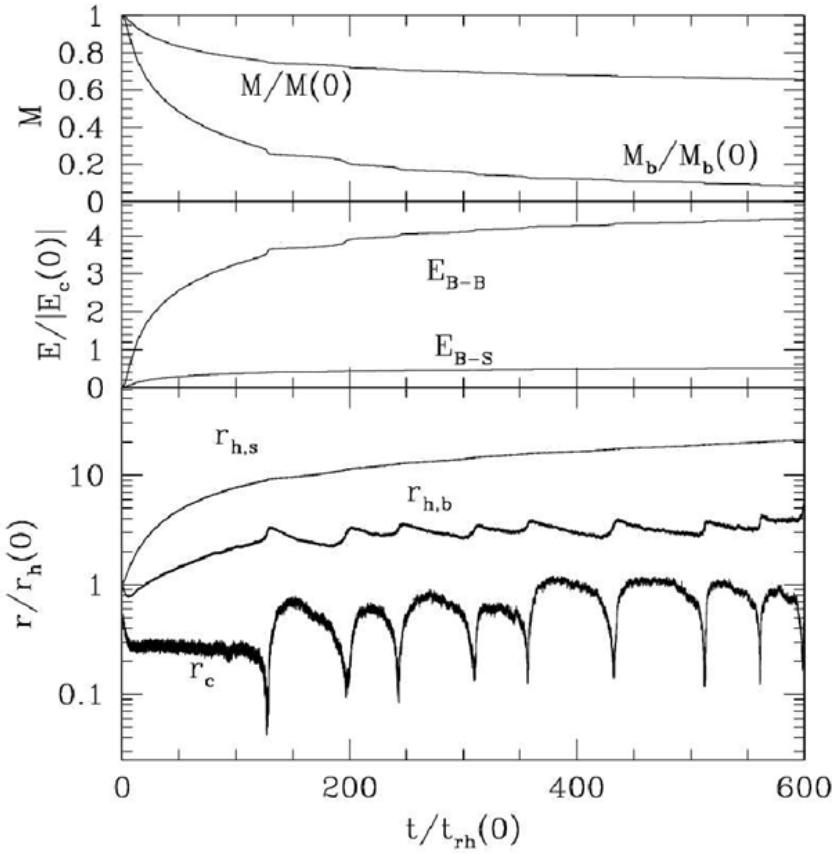

Figure 11: Illustration of core collapse oscillations through binary-binary interactions and interspersed relaxation episodes. From Fregeau et al. (2003), Figure 5

Pertinent explanatory text from Fregeau Figure 5.: 'The top panel shows the total cluster mass, M and the total mass, M_b in binaries. The middle panel shows the energy released through binary-binary and binary-single interactions in units of the original binding energy of the cluster. The lower panel shows the core radius, r_c of the cluster, the half mass radius, $r_{h,s}$ of single stars and the half mass radius, $r_{h,b}$ of binaries. The cluster is initially supported against collapse for about 125 t_{rh}. After the first core collapse, gravothermal oscillations powered by primordial binaries continue up to $\approx 10^3$ t_{rh}. By that time the total number of binaries has been reduced by a factor ≈ 10, but the binary reservoir is still not exhausted. NOTE. The abscissa value of time is in units of t_{rh}, which is the initial half-mass radius relaxation time.' (Spitzer & Hart, 1971).

GC evolution has been investigated to assess the dynamic evolution of the GC central areas concerned with the changes in the binary populations during core collapse, subsequent compression episodes and binary burning (Fregeau et al., 2003; Ji & Bregman, 2015). It is worth a mention that neutron stars, millisecond pulsars and Low Mass X-ray Binaries (LMXB) provide further exotic members of evolving GC core populations. The theory of the creation of a millisecond pulsar is that a neutron star remnant which was created retaining the majority of its angular momentum and forming a rotation powered pulsar, eventually 'turns off'. The remnant returns to a spinning neutron star and is well placed inside the high core density of a GC to attract a giant companion, which sees the recycling label of the scenario satisfied by its spin being increased to a rotation of just under a figure in the region of 10 milliseconds. However this project's concentration is centred on white dwarfs, so for the other objects information is readily available in literature (Tauris et al., 2000; Podsiadlowski et al., 2002; Tauris & van den Heuvel, 2006; Freire, 2013).

As well as the other objects, we see a figure of 57.5% ± 7.9% of blue stragglers in binary systems (Giesers et al., 2019). Blue stragglers are younger, hotter and bluer than the more usually expected members of GCs and they gravitate toward the core of their parent cluster over time due to mass segregation. Their nature has been debated since their discovery in 1953, but the most rational of the explanations is that they are the products of interactions due to the density of their surroundings, where mergers would produce a star more massive than is possible for a stellar population of >10 Gyr. Notwithstanding where, say, two 0.7 $M_{\odot}$ stars merged to evolve, as one would expect, to form a 1.4 $M_{\odot}$ star, in this case it is thought that a blue straggler would remain on the main sequence longer before turning off (Figure 12 below). The existence of blue stragglers demonstrates that the high stellar density can lead to increased interactions (Sandage, 1953; Leonard, 1989).

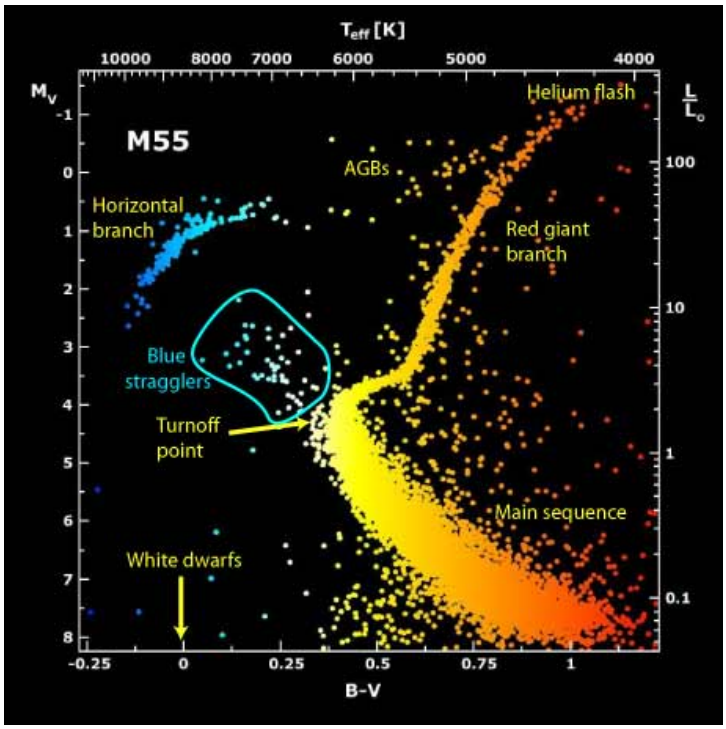

Figure 12: Colour-Magnitude diagram showing evolutionary position of Blue Stragglers. From www.universetoday.com/wp-content/uploads/2008/12/m55cmd

These suggested figures, logically, would naturally lead to mass transfer episodes along with the expectation that these circumstances will eventually produce Type Ia SNe (Pfahl et al., 2009; Voss & Nelemans, 2012).

As a final thought on GC core evolution, modelling and some observations have suggested that high mass dark components exist at the centre of GCs (Taillet et al., 1995; Reynoso-Cordova et al., 2022; Garani et al., 2023). Although the finer detail of these results is still under investigation, there was some indication that either an intermediate mass black hole or indeed a cluster of several black holes have evolved and gravitated toward the GC centre. The dynamics of closely packed black holes suggested that there may probably be some ejection scenarios aided by the low escape velocity during ongoing GC evolution (Vitral & Mamon, 2021), but for the development of this project, black hole influenced binaries are not expected to provide certain impact with respect to Type Ia SNe and are ignored at this stage.

Research thus far, however, has predicted, although not yet recorded, that GCs are very likely to host Type Ia SNe and that remnants of their occurrence exist in observed candidates from the Milky Way GCs, such as the large omega Cen and M22 (Da Costa & Marino, 2011). Investigation has also been carried out to assess the star lifecycle process to ascertain if cluster evolution can be related to the consequential post supernova enrichment of heavy metals. The findings suggest that such enrichment is highly probable to have come from SNe, but further consideration of the gravitational capability of retaining SN remnants is less likely, stating that the larger GCs had more probably resulted from tidal stripping of the nuclei of former dwarf galaxies (Norris et al., 2014). This does not however, detract from the likelihood of SNe occurring whether or not the ejecta remain. This project will search for evidence of Type Ia SN occuring in GCs using data from current surveys. Summaries of the survey missions referenced, more detailed aspects of the methods applied and the associated manipulation of data sourced are outlined below and in later sections as titled.

1.4 Data Sources

This project undertook two complementary searches: it investigated a well understood sample within a chosen volume to allow a thorough statistical analysis of the occurrence rate of Type Ia SNe in GCs; it also examined any Type Ia SN occurring outside this well-defined sample in order to increase the chance of discovering a Type Ia in a GC, at the cost of being unable to robustly statistically determine their frequency.

An initial familiarisation with existing catalogued observations showed that the Zwicky Transient Facility (Bellm et al., 2019) is best placed to provide recent and comprehensive records of Type Ia SN seen during its survey passes (see Section 1.4.1 below). In addition to using the ZTF for finding SNe, the data provided by the PanSTARRS survey was considered most suitable to search for coincidental SN/GC positioning. This due to its spatial coverage being across the same region as ZTF and its archive providing a considerably

greater coadded image depth at a 23.3 g filter magnitude limit (see Section 1.4.2 below). SN detections were not sought from PanSTARRS due to it being less convenient to determine and access a recorded SN event with accurate dating. An introduction to ZTF and Pan-STARRS is provided below in way of an introduction to the missions.

1.4.1 The Zwicky Transient Facility (ZTF)

The ZTF survey is a partnership between the US National Science Foundation and a group of international scientific and academic organisations, which essentially replaces the Palomar Transient Factory (PTF) survey project in California USA (2009 – 2017). It modifies the Palomar Samuel Oschin 48" Schmidt telescope (see Figure 13) imaging optics by the provision of a new wide-field camera of around $47^{\circ 2}$ field of view, utilising the full focal plane area of the telescope, with a readout speed of 8 seconds (Bellm et al., 2019).

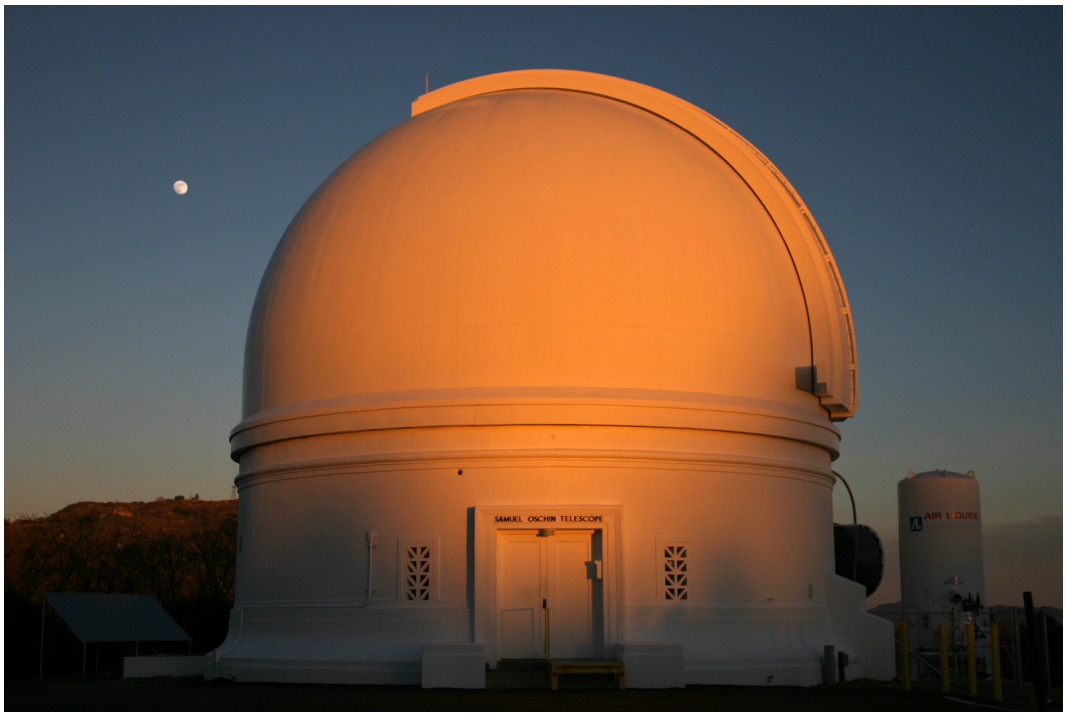

Figure 13: Palomar Samuel Orchin 48" Schmidt telescope dome, California USA
Image credit: Caltech/Palomar

The equipment with the new optics is designed to image the whole of the Northern sky, down to a declination of -27°, every two days with data releases planned for every two months from the processing and archiving facility at IPAC-Caltech (see Figure 14). The limiting magnitude for single images in g filter provides values between 20.8 to 21.1 mag dependent on lunar illumination with a point source 5σ detection limit (Smith et al., 2014; Bellm & Kulkarni, 2017; Bellm et al., 2019; Dekany et al., 2020), so our chosen distance limit of 125 Mpc for SNe inclusion should pose no problem as the apparent peak magnitude of a typical Type Ia SN at 125Mpc is 16.2 in the v-band. We therefore expect an almost complete sample of Type Ia SNe within our survey volume.

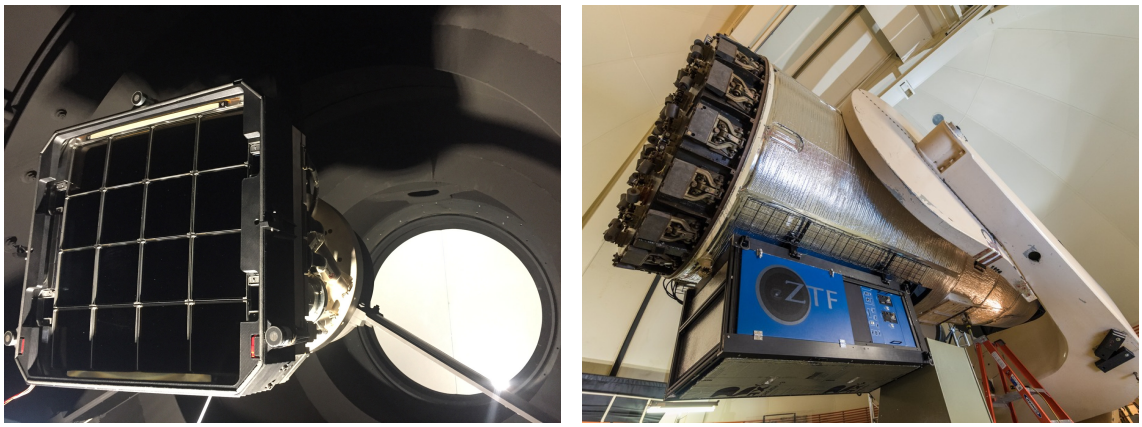

Figure 14: ZTF Camera Installation

The ZTF Wide Field Camera unit (left) and its position on the Samuel Oschin 48" Schmidt Telescope subsequent to installation. Images credit: Caltech/Palomar

CHAPTER 1

The mission looks for several types of transient event including supernovae. The survey data used for this research was initially sourced from the Open Supernova Catalog (Guillochon et al., 2017), however this is now frozen due to a technical problem on 8th March 2022 when the front end database and all programming interaction was lost (see Section 2.1 below). The last script was run on the back end on the 8th April 2022 and no further data was added to the tables [1]. However, the fundamental list of data used in this report was gathered during January and February 2022 from the site, therefore unaffected by the fault. Any related reference and information required was referenced via the Transient Name Server (TNS) (Nordin et al., 2019) site without impact to the original data [2].

[1] https://sne.space

[2] https://www.wis-tns.org

1.4.2 The Panoramic Survey Telescope and Rapid Response System (Pan-STARRS)

Figure 15: Pan-STARRS Facility on the Mountain of Haleakala, Maui
Image credit: University of Hawaii

The Pan-STARRS mission was developed by the Institute for Astronomy at the University of Hawaii and is majority funded by the NASA Near Earth Observation Program. The telescope, PS1, is 1.8 metres in diameter and is fitted with a large 1.4 billion pixel camera, with the facility situated on the island of Maui on the mountain of Haleakala (see Figure 16 below for camera pixel layout). The mission suits the near-Earth requirements because of its wide-field capabilities and the fact that around 1,000$^{\circ 2}$ of the sky is imaged four times during a typical night's work; the multiple exposures provide proper motion and variability measurements.

The available *g r i z y* filters on the optics are able to produce images with a limiting apparent magnitude of 23.3 mag in the g-band with a point source 5σ detection limit when stacked (Finkbeiner et al., 2016; Chambers et al., 2016), so the depth capability is considerable and relatively uniform, which provides confidence in the number of GCs we can expect to see. Also, PS1 is capable of imaging down to a declination of -30° (Chambers et al., 2016), so, in combination with the multiple imaging, it provides perfect alignment to the subject of this report, enabling 'before and after' images of areas where SNe discovered by ZTF have occurred.

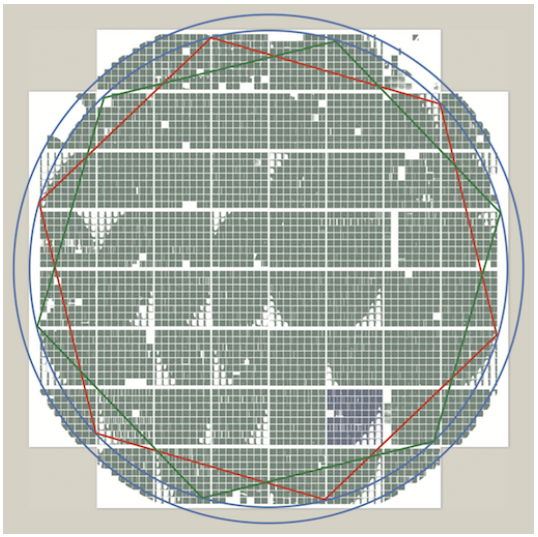

Figure 16: From Fig 3 Chambers et al. (2016)

Gigapixel Camera 1 focal plane layout and mask. Non-functioning cells in white

The methodology and chronological data manipulation is covered in relevant sections below and information on the Pan-STARRS and ZTF missions specifically can be found at the official sites www.ztf.caltech.edu and www2.ifa.hawaii.edu/research/Pan-STARRS.shtml. The base galaxy data to be used in the Pan-STARRS image searches was gathered from the HyperLEDA extragalactic database (see Section 2.2 below) [3], which provides a catalogue of basic galaxy properties for a sample of over 5 million objects.

[3]https://leda.univ-lyon1.fr

1.5 Data Use Methodology

A brief summary of the methodology follows to provide introductory information. A more detailed description of these activities is covered in the data analysis sections below.

Using the ZTF data, the list of SN gathered included their absolute and apparent maximum magnitudes, allowing their apparent distance modulus and distance to be calculated. The list was subject to comparative positional alignment checks with galaxies out to a distance in the region of 125 Mpc (i.e. to provide a buffer for galaxies within the Coma Cluster and to help view the brightest GCs). As stated above, this distance range had been chosen to ensure that a sufficient fraction of the GC population was luminous enough to be detected, as even HST imaging struggles to detect anything but the most massive and rare GCs and Ultra Compact Dwarfs (UCDs) beyond 100Mpc, notwithstanding the 23.3 apparent mag stacked capability of the Pan-STARRS imaging, which converts to an absolute mag of -12.2 in g-band at 125 Mpc compared to the -7.5 Turn Over Magnitude (TOM) in v-band (-7.2 in g-band) from Jordán et al. (2007).

The search for galaxies within the ZTF footprint out to the 125 Mpc chosen distance limit was undertaken from the HyperLEDA database and the individual galactic distances calculated using the HyperLEDA 'modbest' value (see Section 2.3). On constructing the list, an estimation of the number of GCs per galaxy was undertaken. Then, considering the limiting magnitude parameters, using the globular cluster luminosity function (GCLF) and positional coordinates (Jordán et al., 2007; Peng et al., 2008), a figure was obtained for the number of GCs that would be visible in the ZTF and PanSTARRS imaging.

The distances to both the individual SN and its associated galaxy provided an additional check, which would allow confirmation of spatial coincidence between them.

Once assessed, the potential alignment candidates were viewed on the Pan-STARRS image collections to ascertain SN alignment with an imaged point source, which may potentially have been a GC (see Section 3.1). Where available, HST images were also viewed as these tend to be substantially deeper than the ground based photometry.

Chapter 2

DATA SEARCHES

2.1 Search for Supernovae

Data from the the ZTF was requested via a search of the Open Supernova Catalog which contains records of SN data from all sources. The catalogue provides comprehensive data, including light curves and spectra (Guillochon et al., 2017) which could be accessed online until 8th April 2022 (see Subsection 1.4.1 above), however for this project, photometric information for SNe was not necessary to be collected at this stage, concentrating primarily on magnitude, positional and discovery date data of Type Ia SNe.

Considering the survey limitation of Northern hemisphere scans down to -27°, a search criterion was chosen for the most applicable request, which was to provide ZTF specific discoveries of Type Ia SN only, the declination coverage from +90° to -27° was an instrument imposed limit, so there was no need to adjust that range. In addition, the columns chosen for the list were as follows: the specific SN number; the ZTF unique identifier; the discovery date; the maximum apparent magnitude; the maximum absolute magnitude; RA and DEC (both degrees). Distance information was calculated using the recorded apparent and absolute magnitude values and added to the dataframe.

A preliminary sample of 3,637 Type Ia SNe was collected from the catalogue.

It was noted that 14 of the SNe did not have apparent or absolute magnitudes, so these were ignored in the subsequent analysis.

The number of Type Ia SNe within the survey footprint now numbered 3,623. However, as will be covered in more detail later in this report, subsequent to reductions in the total data after statistical limitations, incomplete data and some spurious inclusions, the number was substantially reduced to 307 (see Section 2.5).

2.2 Search for Galaxies

Basic galaxy data were requested via a search of the HyperLEDA extragalactic database, which provides tools to enable study of the physics of galaxies and cosmology. It was started in 1983 and is currently maintained by a collaboration between Observatoire de Lyon in France and the Special Astrophysical Observatory in Russia. The project collects data from literature and surveys to form a homogeneous collection of information enabling scrutiny of objects at different distances. Further information can be found at the official site mentioned in Footnote 3, Section 1.4.2.

To ensure standardisation of the data collected and to facilitate manipulation, filters were applied to the HyperLEDA SQL search option initially to ensure the distance limit of 125Mpc and the maximum declination of -27° were maintained. From there, specific filters were chosen from a list of astrophysical parameters designed to provide the necessary base galaxy information. Those chosen initially were: the object name; RA (Hours); DEC (degrees); Galactic longitude; Galactic latitude; Galactic extinction; Effective B-V colour; Morphological type code; Morphological type; Mean Heliocentric radial velocity (v); Actual error on v; Total B mag; B mag error; Total I mag; I mag error; Total U mag; U mag error; Total V mag; V mag error; Best distance modulus (combining mod0, which is the distance modulus suitable for the close galaxies from the distance catalogue where available and modz, which is the redshift distance modulus estimating the luminosity - distance using the redshift); error on best distance modulus; log of apparent diameter

(d25 in 0.1 arcmin); comma separated list of all the designations for the object in Principle Galaxies Catalogue (PGC) number. Selections and usage of these initial values were dependant upon their application to the further requirements of the project.

A preliminary sample of 71,014 galaxies was collected from the catalogue.

Using the available returned data an initial cull of 7,326 galaxies was carried out on those that did not have values for m_B and m_V or a best distance modulus figure, for the same distance measurement reasoning as for the SNe .

The figure remaining subsequent to that operation was 63,688 galaxies.

2.3 Initial assessment and use of preliminary data

To provide a visual record of the galaxy and SN targets, a projection was built which shows the coordinate positions from the catalogues, with coordinates in degrees, for the full sample of the targets. The filamentary structure of the galaxies was clearly seen and the overlaid positions of all ZTF Type Ia SNe illustrated their distribution pattern.

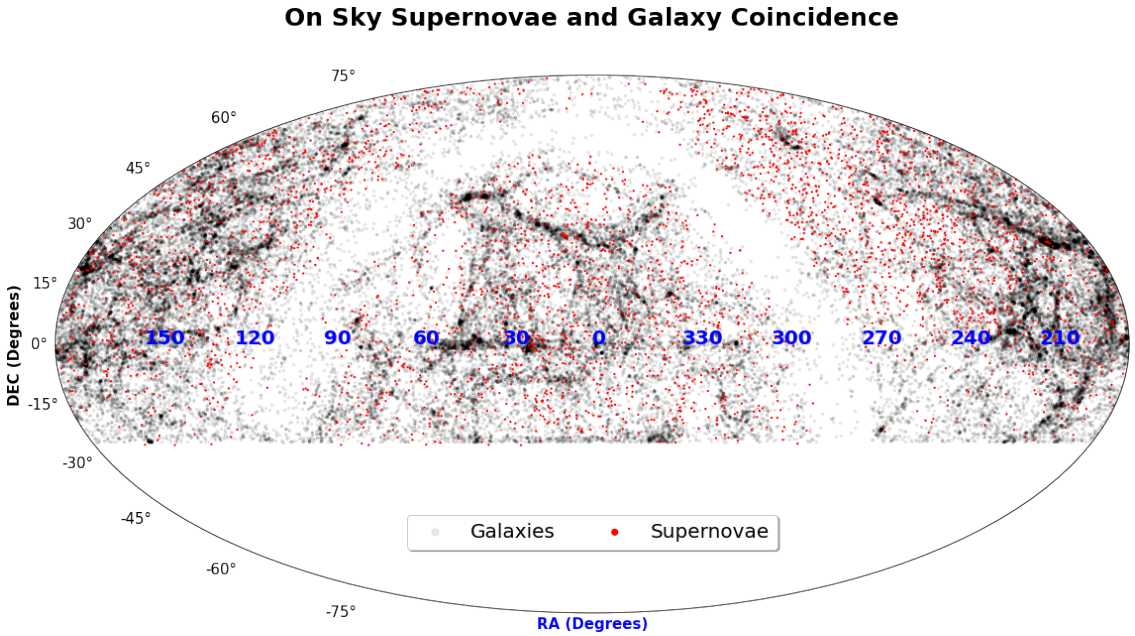

Figure 17: Positions of full sample of target galaxies and SNe Type Ia

The distances of the SNe were calculated from the distance modulus equation, using the apparent and absolute magnitude values from the catalogue, and entered into the dataframe.

For the galaxies, all values of m_B for the remaining 63,688 were available and we also had an associated figure for m_V values being available for 2,954 galaxies out of the total. However, subsequent calculations for the number of GCs required use of absolute magnitude in the V-band, M_V, so a linear relationship between apparent magnitudes m_B and m_V was found from the 2,954 galaxies that had both values available (see Figure 18 below) and this was applied to the remaining m_B values to estimate the missing galaxy m_V magnitudes.

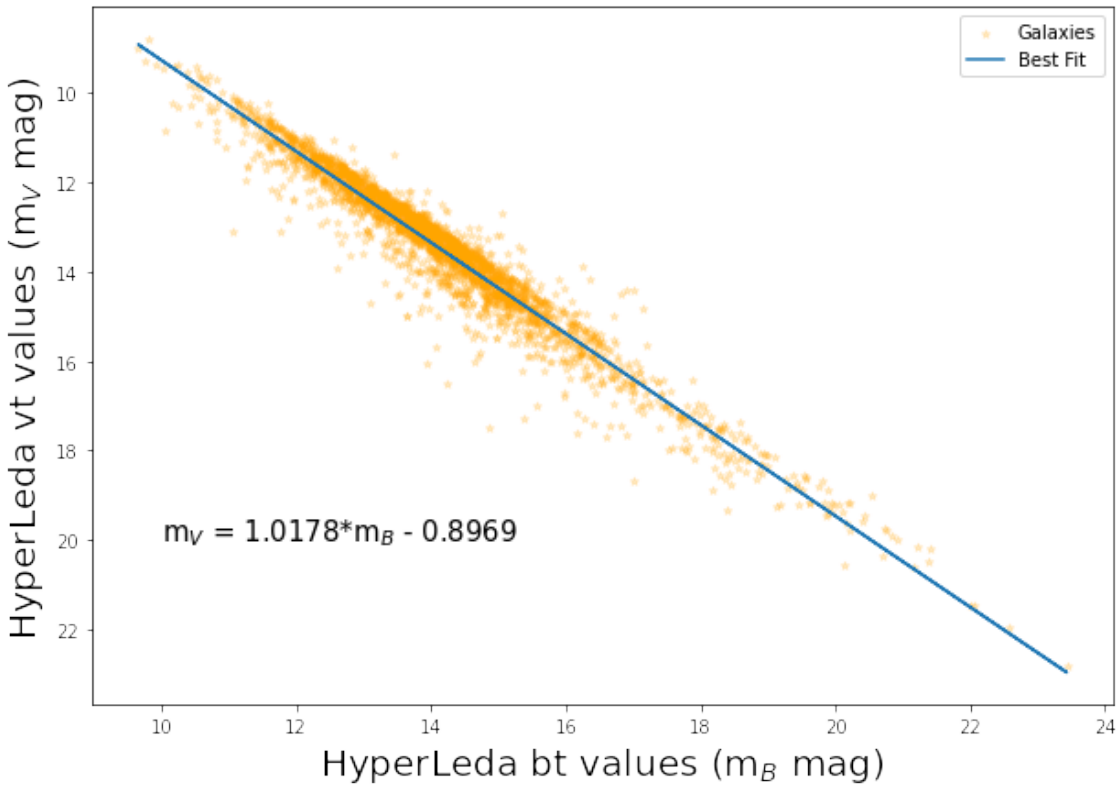

Figure 18: m_B to m_V relationship plot

Using the HyperLEDA 'modbest' figures provided by the search, the estimated magnitude values for M_V, where they were missing, were calculated and added to the dataframe by using the distance modulus relationship, $M_V = m_V$ - 'modbest'. This was necessary to aid in the subsequent estimation calculations of GC numbers at each galaxy.

The 'modbest' value from HyperLEDA available astrophysical parameters is given as 'the best distance modulus', combining distance moduli from distance measurements (mod0) and cosmological distance modulus (modz) as explained in Section 2.2 when detailing the requested HyperLEDA data. As 'modbest' had already been used for magnitude calculations, for consistency it was also used for distance calculations.

The resultant list of data, now including M_V, allowed the progression to assessing how many GCs would be visible within the limiting ZTF and PanSTARRS magnitudes, with a concurrent assessment of extinction effects to be considered as the statistical analysis progressed. So the following section outlines the method used for finding the number of GCs expected at the galaxies provided by the HyperLEDA search.

2.4 Statistical Basis of Globular Cluster Numbers

The full list of galaxies of 63,688 was retained for use in their cross-matching with SNe within a radius of 3 × (logd25/2) (note that this is half of HyperLEDA value, 'logd25' and not the galactic axis ratio logr25 value presented in the database - hence our use of logd25/2), which is detailed in the following sections. This value was chosen to ensure the target SNe association with the galaxy was one of high confidence.

To note, was the fact that the list of galaxies included some that had no value for logd25, which negated their use in subsequent calculations. The rejected galaxies were almost exclusively low mass galaxies with negligible GC populations. These galaxies were removed from the list to leave 56,903.

In order to confirm the robustness of the search radius choice, we investigated the scaling relationship of our range with the effective radius of the galaxy, R_e, where 50% of the galaxy's light is seen hence also known as the half-light radius. This relationship provided an indication of how far out the range is from the centre of our target galaxies. The values for R_e were found by first retrieving values of R_{50} and R_{90}, the radii where 50% and 90% of the Petrosian flux is enclosed respectively (Shen et al., 2003), where available from the SDSS catalogue in the VizieR database. Using the approximation in terms of the Petrosian flux values from Graham et al. (2005):

$$R_e = \frac{R_e}{1 - P_3(R_{90} \div R_{50})^{P_4}}, \text{(where } P_3 = 8.0 \times 10^{-6} \text{ and } P_4 = 8.47\text{)},$$

we were able to plot the approximate scaling for (logd25/2) and R_e thus:

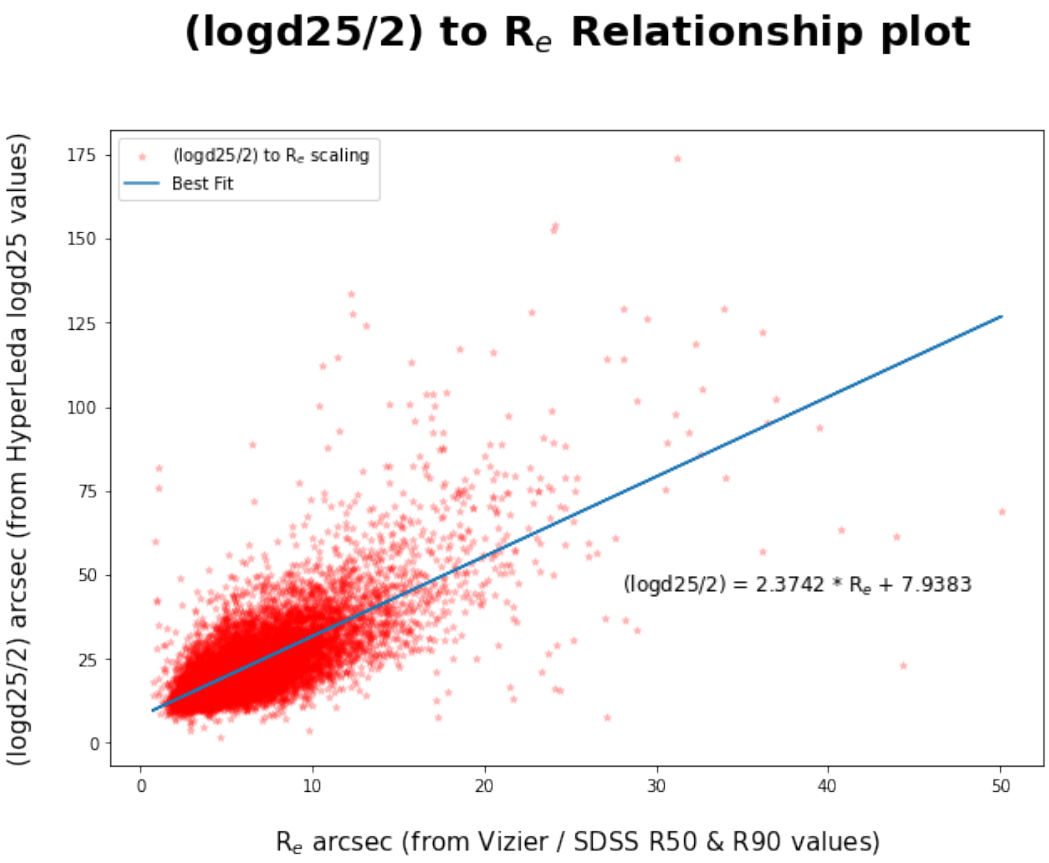

Figure 19: Approximated scaling relationship between (logd25/2) and R_e

We can see that the best fit fraction is approximately 2.4, notwithstanding a median skew caused by some high R_e outlier values in the less dense areas of the plot, putting our range out to almost 7.5 $\times$ R_e, which is a considerable distance to expect any GCs to be observable. Also, that this R_e will contain the vast majority of GCs physically bound to the galaxies without the risk of a bigger radius providing many false events not related to them.

As mentioned above, galaxies can host systems of GCs numbering up to tens of thousands. When a GC system is observed around a galaxy, the histogram of the absolute magnitudes of the collection of individual GCs is seen to form a shape reasonably similar to a Gaussian distribution. This is considered to be consistent across galaxies after observation and has been labelled the Globular Cluster Luminosity Function (GCLF). It is seen to have a peak of $M_V \approx -7.5$ (Jordán et al., 2007), which is termed the Turn Over Magnitude (TOM) and this consistency has led to the GCLF being used as a standard distance indicator. The terms in the associated Gaussian function:

$$\frac{dN}{dm} \sim exp\frac{-(m - m_0)^2}{2\sigma^2},$$

enable the investigation of several values pertinent to this project, viz., dN is the number of GCs in an apparent magnitude range (or bin), dm; m_0 is the TOM and σ is the distribution width (Richtler, 2003; Jordán et al., 2007).

So, to examine the expected number of GCs around our list of HyperLEDA galaxies, we use an established fundamental value termed the specific frequency, S_N, which is the number of GCs observed, N_{GC}, per unit luminosity of the galaxy, normalised to a galaxy with an absolute v-band magnitude of -15. The observation records available at the time of its compilation were predominantly in the V-band and so the value of -15 is based there. Our earlier calculations performed to find the apparent value, m_V, had been used with the HyperLEDA 'modbest' values to find the absolute value, M_V, of our list of galaxies.

This was used in order to find the S_N for each galaxy and therefore progress to having a number of GCs expected at them using the above mentioned established relationship:

$$S_N = N_{GC} \times 10^{0.4(M_V+15)},$$

which enables the manipulation of data to find the S_N relationship with M_V in order to find N_{GC} (Harris & van den Bergh, 1981; Elmegreen, 1999; Peng et al., 2008).

To begin with, we needed to use data available which would allow us to find the above mentioned S_N - M_V relationship. Figure 2 in Peng et al. (2008) (Figure 20 below) shows S_N as a function of M_V in their sample of 100 galaxies, with the value bins given in Table 3 of Peng et al. (2008) (Table 1 below).

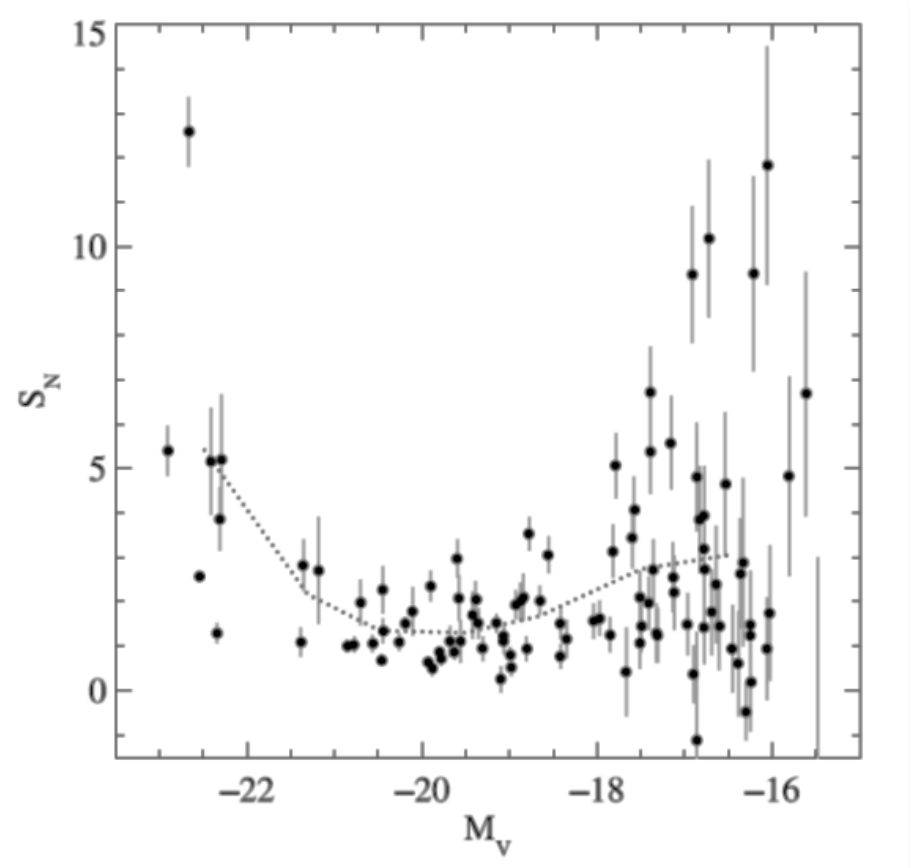

Figure 20: Figure 2 from Peng et al. (2008). Illustrating sample S_N - M_V relationship.

TABLE 3

SPECIFIC FREQUENCY IN BINS OF M_V

M_V Range	$\langle M_V \rangle$	S_N
(−24, −22)[a]	−22.5	4.0
(−24, −22)	−22.5	5.4
(−22, −21)	−21.3	2.2
(−21, −20)	−20.5	1.3
(−20, −19)	−19.5	1.3
(−19, −18)	−18.7	1.7
(−18, −17)	−17.5	2.7
(−17, −15)	−16.4	3.1

[a] Not including VCC 1316 (M87).

Table 1: Table 3 from Peng et al. (2008), bin values for sample from Fig. 20 Above.

We plotted the values from Table 3 (ibid) ignoring the outlier M87 figure, whose inclusion puts our S_N figure for the range -24 to -22 at 5.4 (preferring to maintain a more standardised data set without an outlier with S_N value of 4 in the relationship) and progressively assessed 5 polynomial models to the points before choosing the best fit as illustrated in Figure 21.

The error bars are the statistical errors from Peng et al. (2008) using the seven bins making up the 100 target galaxies from their Tables 1 & 2, with the M_V value from their Table 3 (our Table 1 above) being the mean of each bin and the numbers in each as 7, 3, 10, 18, 13, 19, 30 galaxies respectively. The corresponding S_N values from Peng Table 2, were used to discover the standard deviation in each bin which was then used as the error for that bin shown in Figure 21 below.

Interestingly, the M87 outlier figure being ignored provided a notable query on the estimated number of GCs around it after performing the requisite calculations. More detail of this is given in Section 4.3

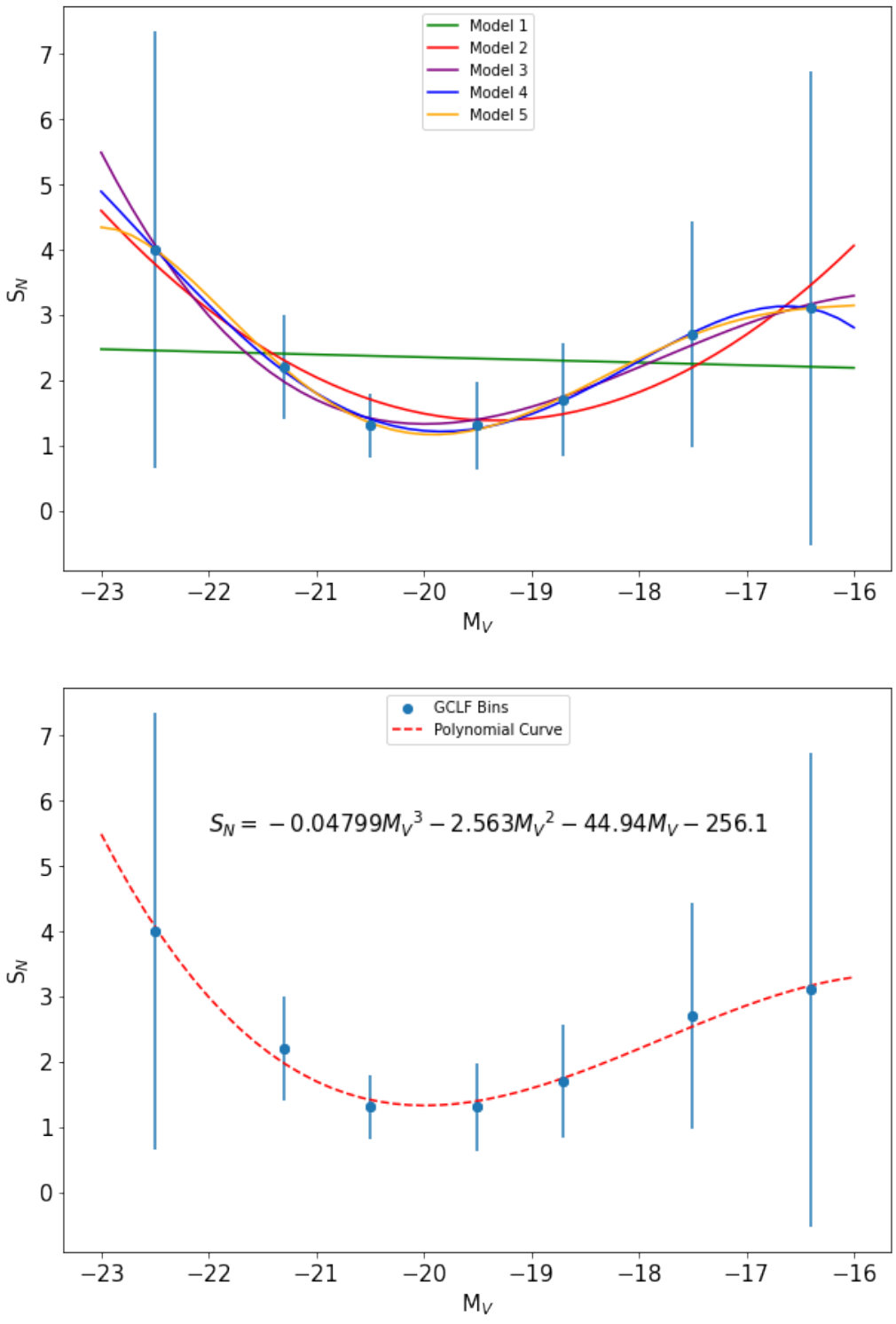

Figure 21: S_N - M_V relationship. Progressive assessments (top) Best fit choice (bottom) Errors bars are from statistical S_N errors in sample bins from Peng et al. (2008)

Model 3 (purple) was chosen with r^2 value (coefficient of determination which measures how well a model predicts an outcome, with unity being perfect) of 0.964, providing the relationship:

$$S_N = -0.04799(M_V)^3 - 2.563(M_V)^2 - 44.94(M_V) - 256.1,$$

The earlier calculated M_V values of the galaxies on our list were then used in the model to find the S_N values of each, adding them to the dataframe.

Then, using the now complete sets of values, we returned to the S_N - N_{GC} relationship above and rearranged to provide:

$$N_{GC} = \frac{S_N}{10^{0.4(M_V+15)}},$$

allowing the number of expected GCs, N_{GC}, at each galaxy to be calculated and in turn also added to the dataframe.

The total number of GCs estimated to exist around the target galaxies was 8,265,578.

From there, as introduced earlier in this section, we know the GCLF histogram of magnitudes of the GCs around a galaxy forms close to a Gaussian distribution (Jordán et al., 2007; Peng et al., 2008), we can begin the statistical analysis of that distribution by using eq. 18 of Jordán et al. (2007) to find its distribution spread, σ. We also need to apply the apparent magnitude to its mean value to enable a correlation to the limiting apparent g-band magnitude of the PanSTARRS survey of 23.3 (see Section 1.4.2 above) when calculating how many of the GCs are not cut off by that limit.

So, we have eq. 18 from Jordán et al. (2007) which uses the absolute b-band magnitude, our M_B value from HyperLEDA 'mabs', to estimate the spread inferred by its linear relationship with σ_g (see Figure 9 in Jordán et al. (2007)). Using the mabs values, we find σ_g with:

$$\sigma_g = 1.14 - (0.1 \times (M_B + 20)),$$

followed by the mean, μ_g, from the GC mean absolute TOM, μ_G, of -7.2 as eq. 19 from Jordán et al. (2007) (note that this value is in the g band to maintain consistency with μ_g and σ_g used in Figure 22 below and not to be confused with the equivalent -7.5 TOM v band value used for the earlier GC number calculations) and the HyperLEDA distance modulus values, 'modbest':

$$\mu_g = (modbest) + \mu_G.$$

The distribution spread and mean values for GCs expected to exist around each galaxy were added to the dataframe to be used in the probability and number of GCs being seen within the limits of visibility.

In order to provide a high level figure for confidence in the number of GCs estimated to exist around the galaxies we adapted the use of the HyperLEDA 'modbest' value once again to maintain consistency. We were provided with the associated 'modbest' error ('e_modbest') figure in the HyperLEDA submission returns and we used that as a confidence range in a Monte-Carlo simulation that takes cognisance of the distance uncertainties thrown up by peculiar motion at low redshifts (Kaiser, 1987; Davis et al., 2011). After assessing the results, we were able to attach an uncertainty figure of 2.6% on the number of GCs estimated.

To consider the visibility limits, the mean, μ_g, and distribution spread, σ_g, of the GC magnitudes were used to generate a normal distribution curve illustrating the volume of GCs under the curve and the position of the apparent g-band magnitude limit of 23.3 as well as the equivalent apparent value corresponding to the GC absolute magnitude value, μ_G, of -7.2. This was produced for a selection of galaxies as a visible precursor to applying the cumulative distribution function (cdf) to the whole galaxy list. The cdf shows the probability of an event happening below a reference value within a range of values by calculating the integral there and allowing the proportion of the overall events limited at that point to be discovered. So we were able to apply the 23.3 limiting g-band magnitude to the analysis and discover the number of GCs probably visible from the proportion of the N_{GC} value, which is represented on the sample distributions as the tail beneath the limiting magnitude. An illustrative example of generated curves is provided in Figure 22 below to show the differences between expected GC numbers in galaxies with diverse parameters.

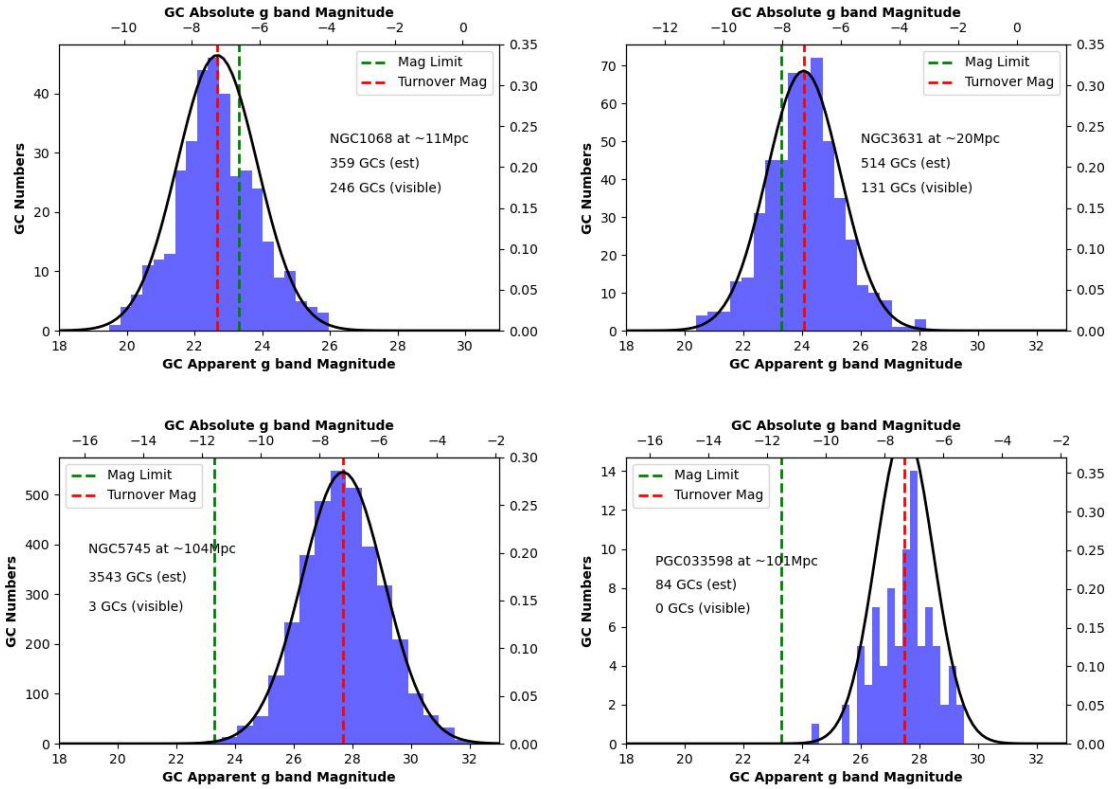

Figure 22: Selection of generated Gaussian curves to illustrate the expected number of GCs visible.

Throughout the project, the figures generated by the work as it progressed were compared with those in the reference literature to provide a check on consistency. As the GCLF was a primary factor in estimating the number and details of the GCs around the target galaxies, an alignment check was made between the collected project data and one selection from the list of 89 galaxies from Jordán et al. (2007). A galaxy from Table 2 in the paper was used from mid range of the list (46 of 89), which was VCC1178, or also NGC4464. The list of galaxies from the project also had this entry, so a comparison was made of the associated data.

From Jordán: VCC1178: 13.37 m_B; 23.609 μ_g; 0.997 σ_g; 90 N_{GC}; 14.6 Mpc; 30.82 mod.
From Project: NGC4464: 13.46 m_B; 23.577 μ_g; 0.907 σ_g; 45 N_{GC}; 15.7 Mpc; 30.98 mod.

The values are seen to align relatively closely. However, the number of GCs is an issue, which may be attributed in consequence of the deeper photometry of the HST data used by Jordán et al. (2007), the contrast in calculated mean value in order to arrive at the predicted number of GCs and the distance difference attributable to the methods used by HyperLEDA and the ACSVCS to arrive at their data.

The initial number of GCs estimated to be visible within the 23.3 limit was 50,763, however further rationalisation was needed on the randomly generated list to check for spurious statistical values. As the mean value was set and fixed to the TOM, the focus was on the distribution figure, σ_g, and a maximum GC magnitude figure to trim outlier values to leave a more rational range. The magnitude was set at ≈-13 M_g, similar to the upper magnitude limit of M_v = -13 suggested by Norris et al. (2014), which would include all Milky Way GCs and allow for the larger, brighter GCs found around massive galaxies. The σ_g values contained some spurious negative and zero entries, which were ignored and culled, with a set limit of 1.4 to provide a set of results that would fall in line with the methodology used from Jordán et al. (2007). The reasoning applied here was with reference to Figure 9 (bottom) and Table 2, both from Jordán (2007), where it can be seen that the majority of σ_g values fall below the plot value of ≈1.35. However, the mean of error values from Table 2 was ± 0.216, so the limiting value was set at σ_g = 1.4 to take cognisance of the upper error. Subsequent to the adjustments of g-band TOM mean, dispersion and magnitude, a figure of 31,679 GCs remained: a figure of much less than 1% of the total of 8,265,578 estimated above (≈ 0.3%).

The figures of principal objects remaining after the above rationalisation and prior to cross-match were now 56,903 galaxies with an estimated 31,679 visible GCs and the now reduced number of 307 SNe (see Section 1.1).

2.5 Cross-match of Supernova and Galaxy Lists

There now was a list of 56,903 galaxies and a list of 3,623 SNe from which a check was carried out to assess which of those SNe occurred near a galaxy within a reasonable radius. The distance measurement chosen was based on the HyperLEDA parameter logd25, explained in the HyperLEDA notes as *'The decimal logarithm of the length of the projected major axis of a galaxy at the isophotal level 25 mag/arcsec^2 in the B-band'*. The logd25 value provided in the database for that parameter was halved to provide a radius from the galaxy centre. To maintain a confidence in associating the SNe with the target galaxy and hence its GCs, a final dimension for the search radius of $3 \times$ (logd25/2) was chosen as the on-sky circle of interest.

As stated, the galaxy data from HyperLEDA had been scrutinised to reject any entries without logd25 values to ensure the chosen radius was consistently discoverable, which left the number of galaxies to be used in the final cross-match as 56,903. The number of SNe predictably remained at 3,623, however the cross-match would turn up instances where there was more than one of the SNe occurring at a galaxy.

Subsequent to completing the calculations, the resulting $3 \times$ (logd25/2) radius range of distances from the centres of the galaxies on the list were recorded to provide a limit for SN proximity. The instances where SNe occurred inside that limit at a galaxy were noted via a programme which provided a search of the sky centred on a galaxy out to their specific individual $3 \times$ (logd25/2) radius as mentioned above. The resultant galaxy name along with the identification code of the SNe within the radius and the separation between the two were then added to the data that provided the search targets. The distances from Earth to both the galaxies and SNe were already known from catalogue data and recorded.

After running the cross-match, an initial list of 321 galaxies remained, but the statistical parameters in Jordán (2007) states that the TOM decreases by $\approx 35\%$ in dwarf galaxies with $M_B \gtrsim -18$ and also the GC TOM values use the -18 figure in their evaluation, so a

cull of galaxies fainter than -18 left a figure of 314 SNe potentially associated with galaxies in our sample, which was further culled due to spurious distance results including zero values and values not inside the 125 Mpc limit for the final assessment of coincidence. So, eventually the figure was left at 307. To provide a comparative visual record of the final galaxy and SN targets, a further projection was built which shows the remaining target galaxies and SNe at Figure 23 below, which can be compared to Figure 17 from earlier in this section.

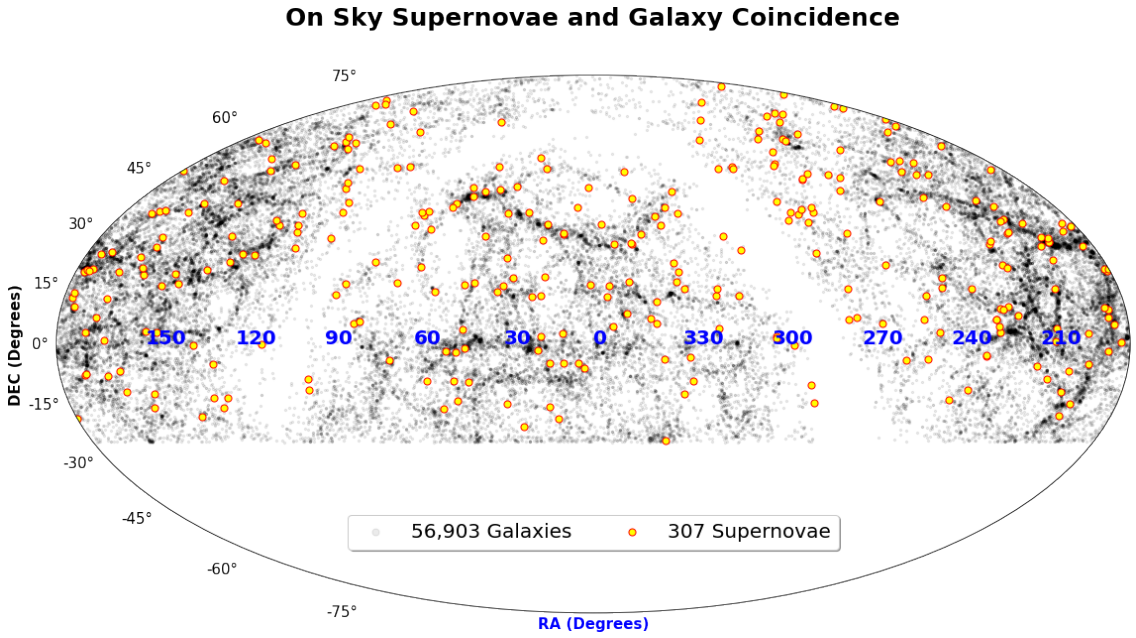

Figure 23: Positions of final sample of target galaxies and SNe Type Ia

Therefore, a final list of 307 SNe remained which had occurred in a location within the 3 × (logd25/2) parameter from a host galaxy within our sample. This list was then used as the reference for visual examination of imaging to assess the spatial probability of coincidence between a SN and a GC. The SNe coordinates were used as the centralised search point for image data from the survey archives to determine whether the SN image from ZTF appeared over a point source from PanSTARRS visible at the galaxy which may be a GC. Thanks to frequent multi-imaging of the ZTF, a date-based 'before and after' view of SN coordinates was available, improving the assessment of coincidence as outlined in the following section.

Chapter 3

EXAMINATION OF COINCIDENCE

3.1 Assessment of Areas of Interest

As a standardisation of image capture sizing between the survey archives, a field of 4 arcminutes square was decided upon for both PanSTARRS and ZTF. In most cases there was a physical difference obvious in the dimensions of the selection of illustrative ZTF image in Figures 24, 25, 26 below, due to the image tiling, however the scale of the images from both surveys and the centralised coordinates of the search were consistent.

The SN coordinates were used for the search submissions in the PanSTARRS archive and the associated image centred on that position was saved for scrutiny. An equivalent search was submitted to the ZTF archive and the images of the position before and after the SN event were also saved for comparison to the PanSTARRS image to check for point sources coincident with the SN position.

As a check on the validity of the astrometrics of the two surveys, a 3 arcsec cone field was chosen and searched in each of them. Due to the increased depth of the Pan-STARRS, more objects were returned from the search there than in ZTF, but the offset of the Right Ascension (RA) and Declination (DEC) measurements between 5 point sources in each were noted and the means and population standard deviation calculated. The results show that the worst case offset mean value was on the RA measurement of just over one tenth

of an arcsec with a very low standard deviation to show that the majority of the offsets are expected to be close to this value. This helped confidence in choosing a figure of 1 arcsec radius when looking for coincidences in the images.

A visual appraisal was carried out on the pairs of images of the SNe remaining on the final cross-matched list mentioned in the last section. This comprised a side by side comparison, with the ability to recall the original catalogued files to allow any magnification of the site along with a search in the HST archive to investigate if a deeper image of the area was available. The coordinates of the SNe are marked by a circular site marker on the ZTF images, which helps to pinpoint the same position with PanSTARRS where no SN was within 1 arcsec in the frame. A further ZTF image prior to the SN explosion was also included in the assessment to show the site based on the potential alignment object only. Where no point source at all was visible either in the images or in deeper archives where available, rejection was obvious. Those possibly of interest that were also rejected were where the SN simply aligned with a galaxy more distant than the limits of the volume and the reshifts of the SNe but still in the image, so it can be safely assumed they aren't associated with a GC. Also rejected were those SNe seen in a galaxy disc or inside the central areas.

In Figure 24 below, we show some rejected images where the SN is in the spiral arms or the main body of the galaxy. Interestingly, the top image may show a starforming knot at the edge of the disk in the region of the SN coordinates.

From the cross-match targets, 39 of the chosen pairs were viewed as potential areas of interest.

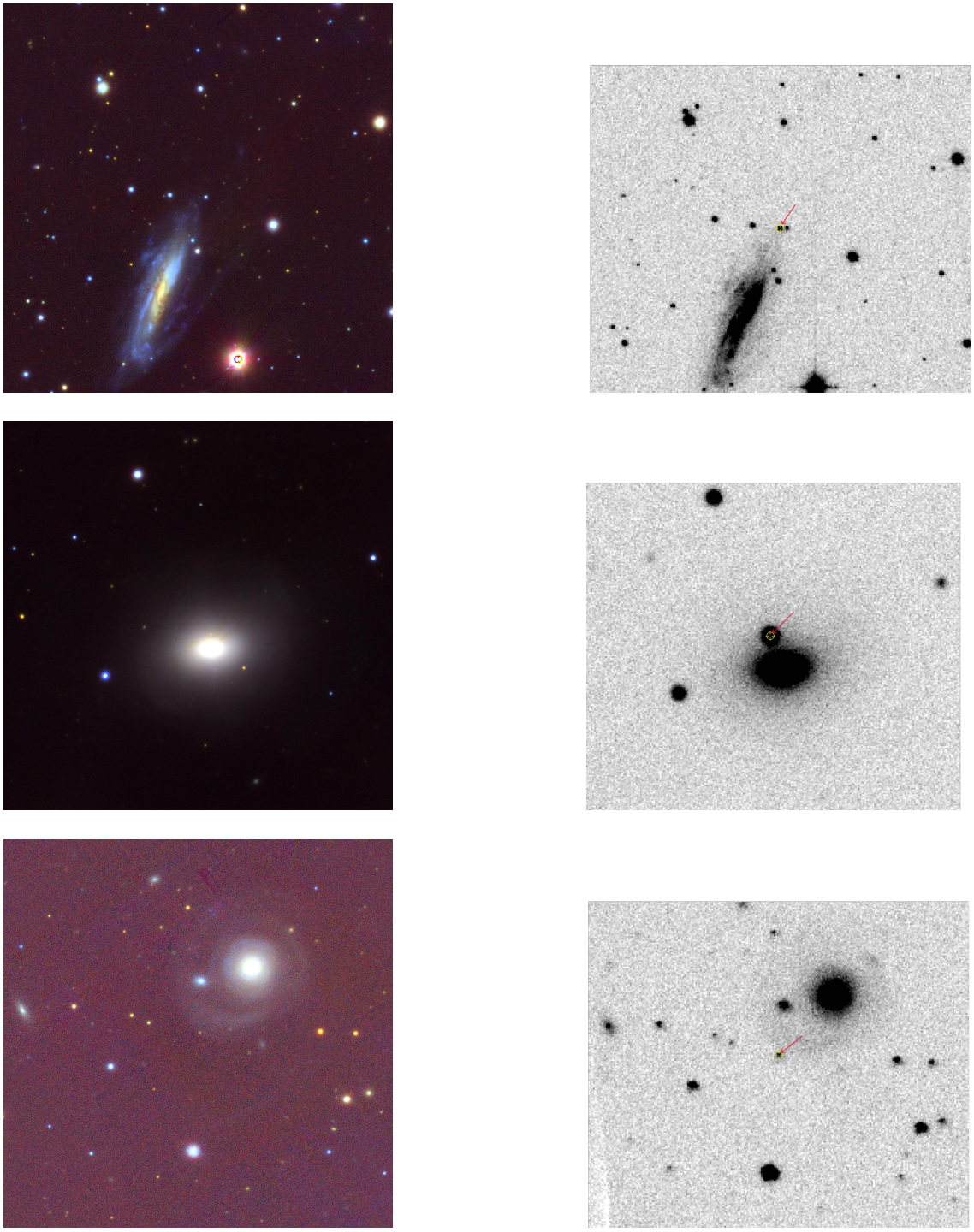

Figure 24: Selection of rejected image files

PanSTARRS Images on left, ZTF Images on right Top: NGC0812; Centre: NGC5018;

Bottom: SDSS J044938.14

3.2 Examination of Three Coincidence Candidates

During the phase of close assessment of the 39 potentially coinciding images, three objects of interest were found to be deemed worthy of further and more detailed individual examination due to the complete alignment of the coordinates on a point source when viewed in the images. The 36 rejected from this final selection were initially found to be a very close match, but not to the extent where the points matched exactly as in the final three candidates. In summary, they comprised a tidal stripping scenario, a remote coincidence and a near galaxy event.

An initial search was requested in VizieR from the Gaia survey, based once again on a one arcsecond radius search around the associated SNe coordinates, which was considered to be a figure which would return the most likely candidate objects. This small area was found to be successful, returning one, three and two possibilities for the three candidates respectively. The results showed that there were no values for distance, parallax or proper motion, supporting the contention that these are distant, probably non-stellar objects. To aid in the assessment, the Gaia coordinates of the candidates were entered in a parallel search in PanSTARRS data, which were used in the scrutiny of its images of the subject galaxies. The apparent magnitudes there were noted in order to provide the necessary photometry to calculate the absolute magnitude in g-band, based on the distance modulus of the host galaxy. The relevant photometry has been recorded in the below Table 2 for reference.

Further imaging for the candidates was checked for both the target coordinates and the potential host galaxy in the HST archives, as HST data can resolve UCDs and cEs at considerable distance, helping to confirm the nature of the objects. However, no data were available for scrutiny and so the exact type of object was still uncertain, leaving the estimation of type to their masses found from the method noted below, which is further explained later in the report.

The first object, noted in the tidal stripping scenario, was more likely to have a definite relationship with the host; however it should be noted that the further two galactic host distances should have caution applied to them due to the possibility that the objects potentially housing the SNe may be objects that just happen to be positioned along the same coordinates, as only spectroscopic follow-up can confirm actual coincidence.

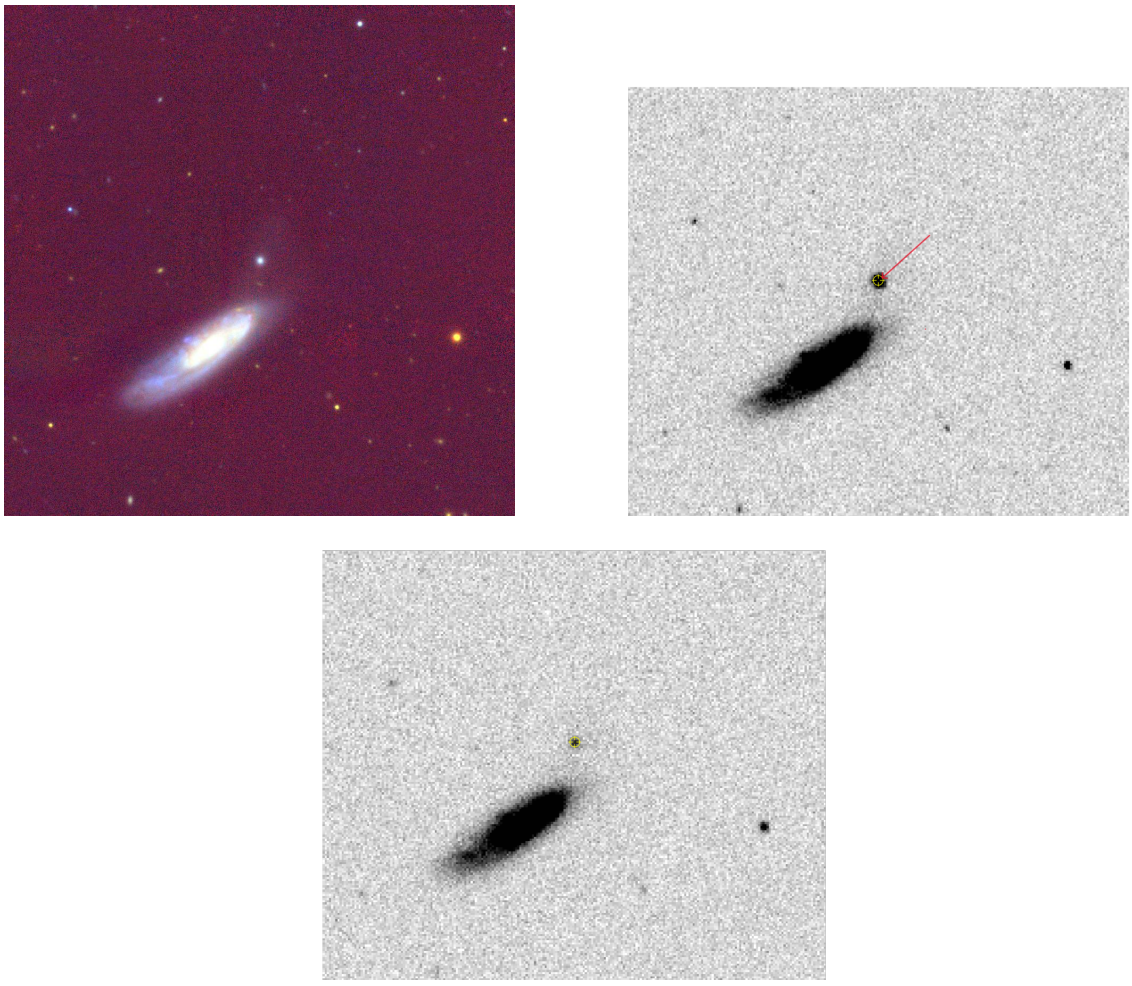

Figure 25: Candidate 1

NGC5243 - PanSTARRS Image left, ZTF Image right. Tidal stripping occuring in elliptical galaxy with SN2019fck in region. Below, earlier ZTF Image shows local area ≈ 7 weeks before SN event

Candidate 1, shown in Figure 25 above, seen to suggest a galactic tidal stripping event as noted earlier, shows the associated SN occurring within the core of the smaller galaxy. The tidal tails confirm that the smaller galaxy (and the SN) are at the same redshift as NGC5243.

The current stripping phase in the galaxy may point to its eventual morphology resulting in a compact elliptical galaxy (type-cE) or an ultra compact dwarf galaxy (UCD) via tidal stripping or 'threshing' (Bekki et al., 2003; Thomas et al., 2008; Norris & Kannappan, 2011; Norris et al., 2014; Ferré-Mateu et al., 2018; Deeley et al., 2023). Both possibilities are of high stellar density in which we would expect to see a proportionately high number of binary systems prone to resulting in Type Ia SNe events.

Notwithstanding the subject matter of this report, the fact that this may not be a GC does not detract from the associated high level of interest. This discovery also further validates that the approach taken in the project works.

Candidates 2 and 3, shown in Figures 26 and 27 below are also of interest, with apparent g-band magnitudes of around 19.7 and 18.6 respectively, they may quite possibly be UCDs with corresponding absolute magnitudes of -14.45 and -15.95, but this needed to be investigated further.

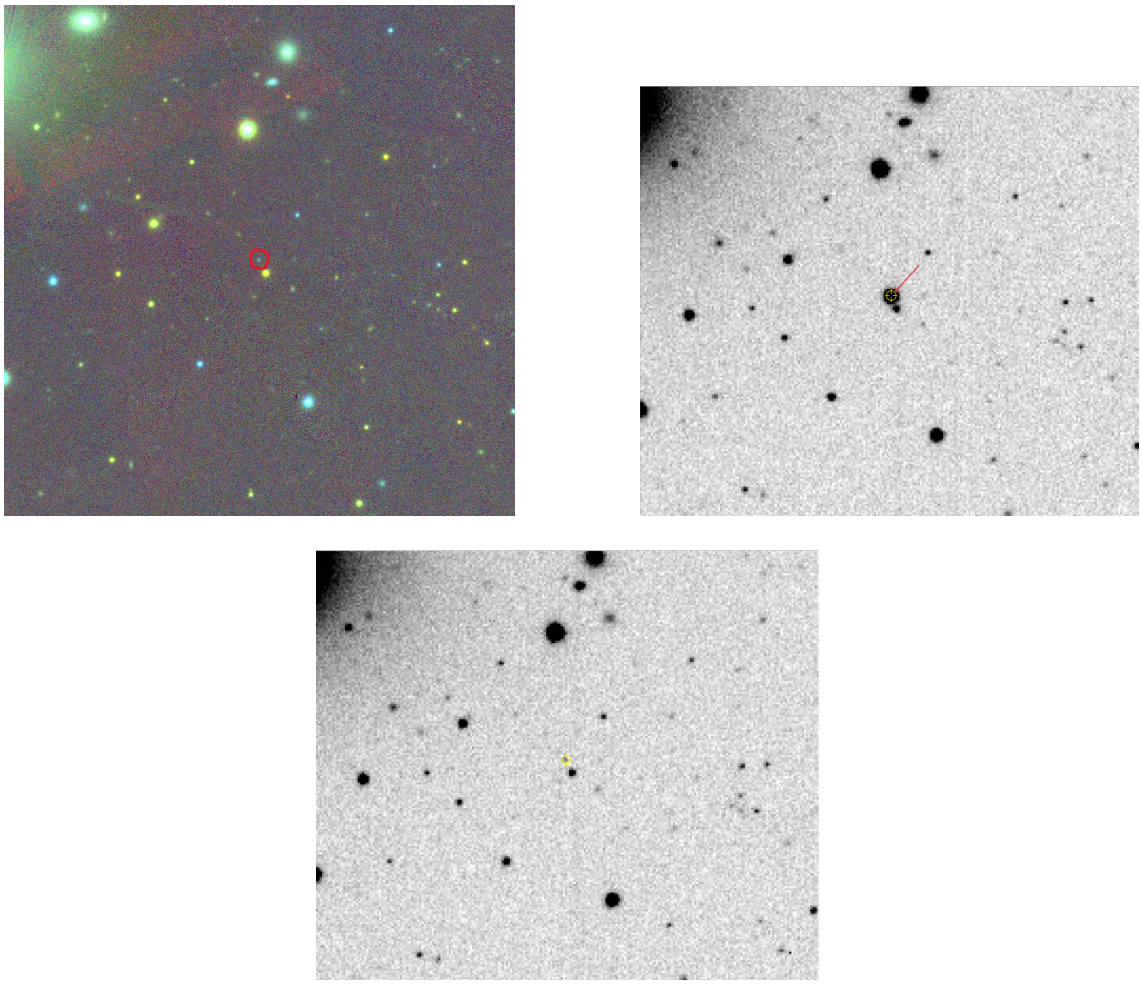

Figure 26: Candidate 2 (red ring)

NGC5111 with SN2020gdw. PanSTARRS Image on left, ZTF Image on right showing SN. Below, earlier ZTF Image shows local area ≈ 6 weeks before SN event

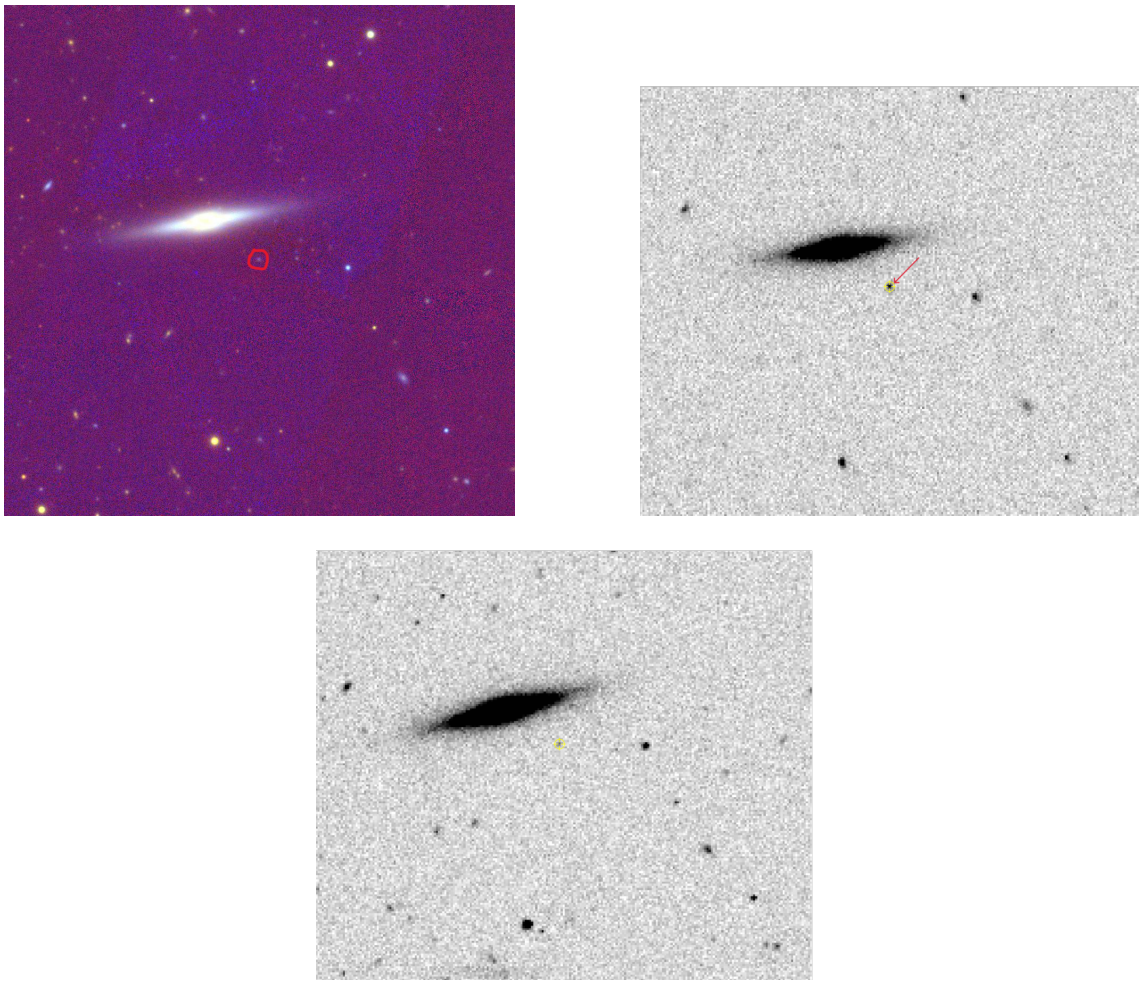

Figure 27: Candidate 3 (red ring)

UGC09543 with ZTFaakswlj. PanSTARRS Image on left, ZTF Image on right showing SN. Below, earlier ZTF Image show local area ≈ 53 weeks before SN event

To provide a basis for discovering what type of object the three candidates may be, their luminosity and mass were estimated using the same method applied to the GCs in the statistical analysis activities outlined in Chapter 4 below. From their absolute magnitudes, the equivalent solar luminosity of the GCs was calculated for each using the g-band absolute solar magnitude of 5.23 (Willmer, 2018)

Subsequently, using the solar absolute magnitude, the relative luminosity of the object was estimated and then its relative solar mass from the mass to light ratio of 3.256 (Maraston & Thomas, 2000; Maraston, 2005), providing two sets of figures. However, the values used for age of 10 Gyr and metallicity of -1.35, as used in the calculation of GC luminosity and mass later in the report, may not be a sound assumption for these potential objects - especially in the case of Candidate 1.

The resulting values for luminosity and mass were as follows:

	Absolute g-band Magnitude	Luminosity / $M_\odot$	Mass / $M_\odot$
Candidate 1.	-14.95	1.08×10^8	3.50×10^8
Candidate 2.	-15.95	2.70×10^8	8.78×10^8
Candidate 3.	-14.45	6.86×10^7	2.23×10^8

Table 2: Comparative magnitude, luminosity and mass values.

Without going into great detail affecting the research basis of this project, the accepted estimated mass of GCs generally lands between a few thousand to over a million solar masses (10^4 to 10^6 $M_\odot$), but for bona fide GCs (i.e. not stripped nuclei), recent papers looking at GC formation history suggest a range of between 10^4 to 10^8 $M_\odot$ (Norris et al., 2019; Fishbach & Fragione, 2023). Masses of UCDs are stated to exist in the range of 10^7 to 10^8 $M_\odot$ when considering the existence of a supermassive black hole in a UCD (Seth et al., 2014; Norris et al., 2019). However, stripped nuclei type UCDs will exist from 10^4 to 10^9 $M_\odot$, but it is simply that they dominate the population at 10^7 to 10^9 $M_\odot$ as very few genuine GCs form at that massive level. Finally, masses of cEs have a solar mass range of 10^8 to 10^9 $M_\odot$ after recent research into their formation pathways (Deeley et al., 2023). So we can see that the PanSTARRS data have all three candidates in the UCD/cE range. However, GCs are gravitationally bound and contain no dark matter, whereas UCDs and cEs have gas, dust, dark matter etc, which will change the mass to light ratio used to gather the data for this project and will need to be investigated going on from here to discover whether the candidates are UCDs, cEs or genuinely large GCs, although the magnitudes in table 2 above initially suggest they are within the UCD regime.

The overall statistical process concerning the results of this project is covered in the following section and the inclusion of the potential candidates will be assessed for any impact on the eventual rate limits concluded from it.

Beyond this report, the three candidates are worthy of investigation and a suitable ground based telescope is to be assessed for a time proposal for spectroscopic follow-up to confirm their nature. Deeper imaging data of those SNe not currently associated with point sources might also be the subject of a request to search for GCs below our current detection limit.

Chapter 4

STATISTICAL ASSESSMENT OF RESULTS

4.1 Consideration of Selected Volume

To determine the volume within which we have surveyed for Type Ia SNe within GCs, we use the previously described distance limit of 125Mpc.

Using the spherical volume out to 125 Mpc from $\frac{4}{3}\pi r^3$, which is 8.181×10^6 Mpc^3 but evaluating and removing the spherical sector volume made by the 'polar cap' from $-27°$ to $-90°$ South added to the cone subtended by sweeping out the volume from the centre of the sphere at a 125 Mpc radius to the $-27°$ parallel, the observed volume is:

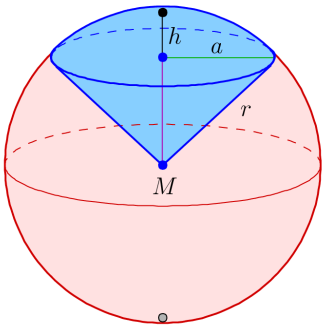

Figure 28: Spherical sector volume graphic definition of terms.

$$\text{Volume of cap} = \frac{1}{6}\pi h(3a^2 + h^2) = 1.497 \times 10^6 \text{ Mpc}^3,$$

$$\text{Volume of cone} = \pi r^2 \frac{h}{3} = 9.285 \times 10^5 \text{ Mpc}^3,$$

Adding both volumes, we get:

$$\text{Volume of sector } = 2.425 \times 10^6 \text{ Mpc}^3,$$

which, when removed from the total volume of 8.181×10^6 Mpc^3 , returned an observable volume of 5.756×10^6 Mpc^3, representing 70.4% of the total spherical volume out to 125 Mpc with latitude limit of -27° to be used in the following analysis.

4.2 Total Stellar Mass Within the Volume

To provide a comparison between the total stellar mass of the project volume and the stellar mass of the GCs within it, we initially find the universal stellar mass density figure and apply it to the earlier calculated volume from above Section 4.1 of 5.756×10^6 Mpc^3.

The figure used for the critical density of the universe of 9.9×10^{-27} kg m^{-3} is from data provided by the Wilkinson Microwave Anisotropy Probe (WMAP) (NASA/WMAP Science Team, 2014). After removing the other mass and energy components (dark matter, radiation, dark energy), leaving only the stars to provide the stellar mass density value, we see from Karachentsev & Telikova (2018) that out to $\approx$ 135 Mpc, the stellar population alone comprises only 0.22 ± 0.02 % of the critical density, which provides us with a stellar mass density figure of 2.178×10^{-29} kg m^{-3}.

The stellar mass density in solar units in that figure is 1.095×10^{-59} M$_\odot$ pc^{-3} or 3.217×10^8 M$_\odot$ Mpc^{-3} out to 135 Mpc. So, using this, we can calculate the estimated stellar mass within the volume used in this project to be: $(3.217 \times 10^8) \times (5.756 \times 10^6) = 1.852 \times 10^{15}$ M$_\odot$. Obviously, our total GC uncertainty figure of 2.6% from Section 2.4 is applicable here.

4.3 Consideration of Volumetric GC Mass Density

The rationale to estimating that a total of 31,679 GCs would be visible, along with the selection that yielded 307 SNe is explained in Chapter 2 with the associated image review to find the 39 areas of interest which eventually provided three final candidates for coincidence.

To arrive at the statistical mass of GCs to be used in the final rate limits, the g-band absolute magnitudes of the 31,679 GCs were calculated from their apparent magnitudes and the catalogue distance modulus.

From the absolute magnitudes, the equivalent solar luminosity of the GCs was calculated for each using the g-band absolute solar magnitude of 5.23 (Willmer, 2018) in,

$$M_g - M_\odot = 2.512 \times \log\left(\frac{L_g}{L_\odot}\right), \text{ providing}$$

$$L_g = 10^{(M_g - M_\odot / -2.512)} \times L_\odot$$

The equivalent stellar mass in solar mass units was then found from the luminosity by multiplying by the mass to light ratio value of 3.256 in the g-band (Maraston & Thomas, 2000; Maraston, 2005), assuming a GC metallicity figure of -1.35, chosen to provide a rough average for GCs which have a metallicity that span the range from -2 to 0 (Jordán et al., 2007) and an age of 10 Gyr, due to GCs being generally old (Gratton et al. 2019 and references therein). GCs all comprise old stars where the ongoing evolution sees the metallicity and mass remain constant.

The resulting 31,679 GC values were as follows:

GC Absolute Magnitude Range	-6.8 to -13.5 M_g
Luminosity Range	6.288×10^4 to 2.918×10^7 $L_\odot$
Luminosity total	3.366×10^{10} $L_\odot$
Mass Range	2.047×10^5 to 9.502×10^7 $M_\odot$
Mass total	1.096×10^{11} $M_\odot$

Table 3: Magnitude, luminosity and mass values of estimated GCs.

We see the total mass of the GCs estimated to be visible around the target galaxies is greater than the estimated Milky Way stellar mass of 6.08×10^{10} $M_\odot$ (Licquia & Newman, 2015), however there is some consideration to be given to the accuracy of the GC estimated figure. It was noted through referencing NGC4486 earlier in the report (Section 1.3) and after the GC number estimate was carried out, that the familiar galaxy NGC4486 (M87) appeared to have a comparatively small number of GCs compared to the generally accepted number.

It so happens that the data basis used by this project in estimating the GC number is that stated in Jordán et al. (2007), using Table 2 as shown in Section 2.4 and adopting the same logic with regards to the choice of the M87 S_N value. Within those data, the true S_N value for M87 is considerably higher than the estimated value used to calculate the best fit to the relation as pointed out in Section 2.4 and that is why M87 is estimated to have fewer GCs than it is observed to have. This may be an issue for many of the largest, but rarest, GC systems and should be considered in any further study.

This suggested that the GC total may be very slightly underestimated notwithstanding our uncertainty figure of 2.6%, but, as a check for further possible anomalies, ten of the known brightest remaining galaxies in the volume (mostly cD galaxies) were checked for

GC estimates and the results varied from 13,000 to over 19,000, so, considering this, it is believed that overall the HyperLEDA magnitudes are basically sound.

It was also seen that as the g band TOM of −7.2 corresponds relatively consistently to a Turn Over Mass of $2.2 \pm 0.4 \times 10^5$ $M_\odot$ (Jordán et al., 2007), we should be able to see that the GC estimation numbers had picked up on the brightest of the galaxies by looking at the solar equivalent masses of the GCs. The histogram in Figure 29 below helps illustrate that this was the case.

As there were 8,265,578 GCs initially estimated to be present in the project volume (Section 2.4 above), we could see that the above Turn Over Mass figure of $2.2 \pm 0.4 \times 10^5$ $M_\odot$ would provide an absolute total figure of 1.818×10^{12} $M_\odot$ in GCs. However, as shown in Table 3 above the remaining GCs are estimated to have a mass of 1.096×10^{11} $M_\odot$. Hence we see that the 31,679 GCs estimated to be detectable comprise only 0.4% of the GCs by number, but 6% by mass, meaning as expected that they are systematically biased toward the higher mass clusters as Figure 29 demonstrates. Our GC number uncertainty figure of 2.6% would have little effect on these proportions.

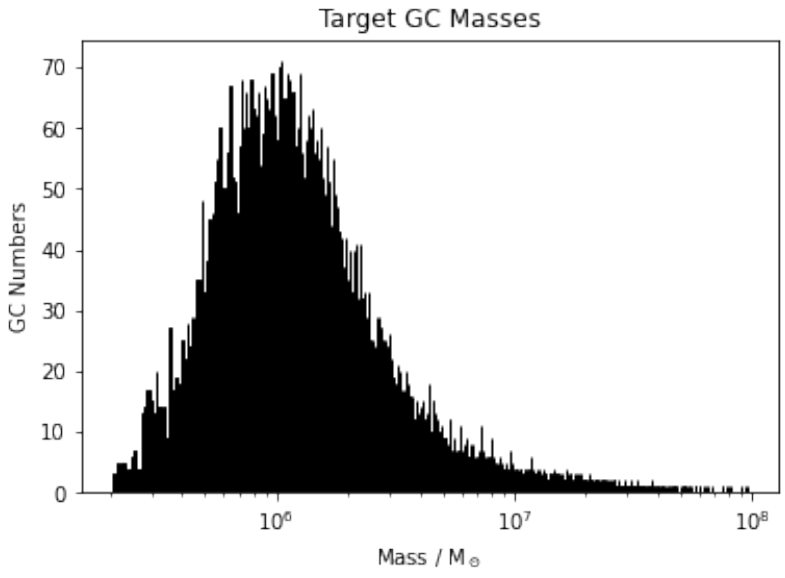

Figure 29: Illustration of estimated GC masses for the remining 31,679 GCs

4.4 Consideration of Volumetric SNe Events

The search requested from the Open Supernova Catalogue returned 3,637 Type Ia SNe. Subsequent substantial reductions of this total were carried out by culling records that had certain parameters missing that were needed during the more detailed application of data later in the project. To ensure a logical assessment of the SNe included in the calculations, 3,330 were removed that had no magnitude values and spurious or out of limit distance values. Therefore, the original number has been reduced here to 307 to calculate the Type Ia SNe event rate in the project volume, because that revised figure provides us with actual events notwithstanding the lack of further information for some more of them which also obviated their eventual later inclusion.

So, as the events were recorded over a period of discovery dates from 8th April 2018 to 20th November 2021, which is the equivalent of 3.62 years, providing us with a figure of 84.75 SNe per year within our volume.

The calculated volume from Section 4.1 above is $5.756 \times 10^6\,\mathrm{Mpc}^{-3}$, so from these estimates we would expect to see event numbers at $1.47 \times 10^{-5}\,\mathrm{yr}^{-1}\,\mathrm{Mpc}^{-3}$.

Similarly, the calculated solar mass in that volume is $1.852 \times 10^{15}\,\mathrm{M}_{\odot}$, so we would expect to see event numbers of $4.58 \times 10^{-14}\,\mathrm{yr}^{-1}\,\mathrm{M}_{\odot}{}^{-1}$.

Considering the recorded SN data in this report is based on the latest ZTF survey findings and some of the earlier research based SNe rates have been based on and before the pre-ZTF Palomar Transient Factory survey data, the above estimates generally are an order of magnitude less than those presented in literature with a volumetric rate of between 1 and $3.5 \times 10^{-4}\,\mathrm{yr}^{-1}\,\mathrm{Mpc}^{-3}$ and a stellar mass rate of 1.12 to $3.5 \times 10^{-13}\,\mathrm{yr}^{-1}\,\mathrm{M}_{\odot}{}^{-1}$(Scannapieco & Bildsten, 2005; Strigari, 2006; Panagia et al., 2007; Ruiter et al., 2009; Maoz et al., 2014; Friedmann & Maoz, 2018; Brown et al., 2019), the exceptions being Frohmaier et al. (2019), who presents a volumetric rate of $2.43{\times}10^{-5}\,\mathrm{yr}^{-1}\,\mathrm{Mpc}^{-3}$, based on three years' observation records by the Palomar Survey and Desai et al. (2024), who presents a rate of $1.91 \times 10^{-5}\,\mathrm{yr}^{-1}\,\mathrm{Mpc}^{-3}$, based on four years' Type Ia observation

records from the V-band All-Sky Automated Survey for Supernovae (ASAS-SN) catalogues spanning discovery dates from UTC 26/01/2014 to UTC 29/12/2017.

Hence, while a little low compared to most similar measurements, our values do lie within the range of those determined previously.

4.5 Consideration of Rate Limits

The data used in finding the number of SNe from the ZTF had been recorded over almost four years when applied to this project, from the initial ZTF survey date of March 2018 to the last set of data in February 2022. The volume used in the collection of observation data with respect to SNe, GCs and galaxies is 5.756×10^6 Mpc^3 from Section 4.1 above. The solar equivalent stellar mass of the project's volumes, estimated in Section 4.2 above, is 1.852×10^{15} M$_\odot$ and within that volume, we estimated a solar equivalent stellar mass of GCs at 1.096×10^{11} M$_\odot$ in Section 4.3 with an uncertainty of 2.6%. The two values obtained for SNe events in Section 4.3 were 1.47×10^{-5} yr^{-1} Mpc^3 and 4.58×10^{-14} yr^{-1} M$_\odot{}^{-1}$.

So, the mass of GCs was surveyed for 3.62 years and from this, due to the fact that no SN was confirmed within a GC with a 100% confidence, we can say that we now have arrived at the lower probability limit figures for the events.

Had we observed one SNe definitely within a GC during the project time of 3.62 years, the upper limit for events within the 31,679 GCs would be 2.52×10^{-12} yr^{-1} M$_\odot{}^{-1}$.

We can see that this figure is two orders of magnitude higher than our calculated rate for stellar mass, so the conclusion is that we wouldn't expect to definitely see a SN in a GC unless they are enhanced substantially compared to normal galaxies. So, from:

$$\frac{2.52 \times 10^{-12}}{4.58 \times 10^{-14}} = 55,$$

we find that we would need to increase the time surveyed, or the number of GCs, by 55 times to be likely to see a SN in a GC.

Future research based on the three candidates detailed in Section 3 will, however, provide the opportunity to revise the figures to take account of the possibility that one or more of them was indeed a GC. Further, should the objects be UCDs or cEs, then other event versus mass comparisons are open for debate.

4.6 Concluding Summary

No SN has yet been recorded within a definitive GC, so this work set out to either find such an event or to provide updated information on the rate limits of its occurrence. The project has worked through a large initial list of SNe and galaxy targets from recorded catalogue data before arriving at a final set of SNe within a reasonable distance from their associated host galaxies. To examine the possibility of a SN occurring within one of the host galaxy GCs, statistical processes were used from referenced literature to ascertain the numbers of GCs at each galaxy and those visible within the magnitude and distance limits set. Images of the final list of SNe were examined along with area images of the SNe coordinates pre-explosion, to record possible coincidental positioning of SNe and existing point sources in the area. No definite coincidences of SNe/GC were noted, but three instances of interest were noted that require further investigation. The initial assessment of their masses suggested they may be UCD or cE objects or perhaps actual very large GCs, but further detailed examination is required to provide more confidence.

It can be seen that there was a continuing phase of the reduction of data as the project progressed. The initial number of 3,637 SNe was reduced by removal of those with no apparent or absolute magnitude figures available followed by those with spurious or no distance values; then, as the ZTF survey has no distance limit, that number was further reduced by the removal of SNe more distant that the project limit. Finally, those SNe separated from the host galaxy by a distance of over the 3 x (logd25/2) figure, or those at host galaxies dimmer than -18 M_B, to maintain the statistical limits within the calculations from Jordán et al. (2007), were also removed leaving a figure of 307 SNe.

The galaxies from the HyperLEDA database numbered 71,014 in the search. The first reduction was the removal of those without apparent magnitude values in b or v, which were needed for distance calculations. Then, as the galaxy to SNe separation calculations required logd25 values, those without were removed from the list. This left a value of 56,903 galaxies.

As the list of galaxies prior to the cuts were bona fide objects, the total number of GCs estimated to exist around them was 8,265,578. This figure was assessed for spurious content and distance variations as outlined in Section 2.4, which suggested an uncertainty of 2.6%, and then used along with the total volume and associated stellar mass when calculating the final overall figures applied to the rates calculated. However, as can be seen from the reduced figures of SNe and galaxies explained above, the rates were based on the number of SNe seen (307) within the project volume. So, the host galaxies of the SNe were used to ascertain the associated visible GCs, which provided a figure of 31,679.

Therefore to summarise, we had 307 SN occurring in a volume where there were an estimated 31,679 visible GCs and the resulting rate limits found from these figures are discussed in the Sections above.

So, the expected mass of visible GCs in the project volume is 1.096×10^{11} $M_{\odot}$ and with a rate of 4.58×10^{-14} yr^{-1} $M_{\odot}{}^{-1}$ estimated from the volume as a whole this provides a figure of 199.22, suggesting we would expect to see a Type Ia SN in one of the GCs around every 200 years.

As a comparison, the Milky Way with its mass of 6.08×10^{10} $M_{\odot}$ produces a figure of 363.9, so in this case we would expect to see a Type Ia SN every 360 or so years.

Chapter 5

DISCUSSION

5.1 Appreciation of Event Relationship

As outlined in the last chapter, a sighting of a SN within the estimated project volume was not entirely expected due to their annual rate with respect to stellar mass of $4.58 \times 10^{-14}\,\mathrm{yr}^{-1}\,\mathrm{M}_{\odot}{}^{-1}$, indicating that a survey period of 200 years would be necessary to detect 1 event given the estimated number of GCs visible.

The GC stellar mass found is larger than that of the Milky Way and it is general belief that Type Ia SN1604, or Kepler's Supernova, was the most recently observed in the Milky Way. Records have valid observations of a presumed Type Ia at 1006 and 48 years later at 1054, although a presumed Type II; then Tycho's Star a Type Ia in 1572, only 32 years before Kepler's Supernova. If history is to repeat itself, then our findings, which show that a Type Ia SN event is to be expected to be around every 360 or so years, indicate another Type Ia SN is overdue in the Milky Way.

This would also apply to GCs if the rates were consistent as in the paragraphs above, however this is a risk filled assumption as the environment and evolution differs between galaxies and GCs. Debris may obscure events in galaxies where perhaps interactions are fewer and ongoing star formation provides younger populations of more metal rich stars, whereas the frequent interactions in GCs may affect the probability of SNe one way or

the other, perhaps increasing the frequency through the hardening of binaries leading to increased mass transfer or reducing it by having 3-body interactions separate, split or even eject stars from binary systems. A further aspect is whether the GCs have undergone a peak of Type Ia SNe events because of the age of the population, being most probably between 10 and 13 Gyr old. At these ages the stars down to $\approx 0.9\,M_{\odot}$ will have evolved off the Main Sequence, leaving mostly sub solar mass stars of spectral type K and cooler along with cooling white dwarfs. Due to this, there may be interactions with 2 stars at 0.7 $M_{\odot}$ that interact and simply make one star of 1.4 $M_{\odot}$. What is needed to produce a Type Ia SN of course is perhaps a long dead 1.2 $M_{\odot}$ white dwarf alongside a 0.8 $M_{\odot}$ which loses 0.2 $M_{\odot}$ to the larger white dwarf which subsequently runs into a Type Ia SN.

The fact is we cannot be confident which way the relationship between galaxies, GCs and SN goes, hence the continued interest in studies such as this, which seek to measure the SN rate in different stellar populations. Consequently, the three candidates uncovered during this work will be followed up on, to assess the possibility of finding a yet uncovered parameter.

As noted above, during the work there were some interesting items uncovered, detailed in Chapter 3, that will see more investigation. The potential proto UCD/cE Candidate 1 is definitely undergoing tidal stripping and the fact that no SN has been recorded in a cE makes this an interesting object. The further two, Candidates 1 and 2, could also be cEs or UCDs or even extremely large GCs, where a record of finding the lowest mass object housing a Type Ia SN is a possibility. All will be looked into as ongoing research, which bodes well for the future using the upcoming improved equipment outlined below.

5.2 Future Research

We now look forward to the next phase in the continuing research with improved technology, which sees the use of the Legacy Survey of Space and Time (LSST) at the Vera Rubin Observatory in Chile. The LSST project will see the Earth-based telescope perform a 10 year survey, imaging the observable sky once every four nights through its 8.4 m telescope with a 3.2 gigapixel imaging device which will produce single r-band images up to 24.5 mag and stacked images up to 27.8 mag (LSST Science Collaboration et al., 2009; Ivezić et al., 2019).

To illustrate the improved data capture from the LSST, the targets are to image 20 billion galaxies and 17 billion stars (Hernandez et al., 2023), taking the possibilities of arriving at a much more detailed Type Ia SN/GC event occurrence rate far beyond any estimates to date. Expectations are already high and referring back to our consideration of peculiar velocity related distance variations at low redshift in Section 2.4, Odderskov & Hannestad (2017)'s work show they are looking forward to its data releases.

Benefiting such research, the ZTF survey, used for this project with its recorded 3,637 SNe events, has been upgraded to the ZTF Bright Transient Survey, to provide the largest spectroscopic SNe survey thus far. By the end of 2024, it is targeting 10,000 SNe spectra records of those brighter than 18.5 mag (Fremling et al., 2020; Perley et al., 2020).

Therefore we can see that the LSST has an improvement of 4.5 magnitudes on the limit of this project, which suggests a multiple of $2.512^{4.5} = 63$ aplied to the objects recorded in the work. So the improvements promise to provide 63 times the objects we had expected here and therefore somewhat less than 63 times the mass due to already preferentially having the brightest GCs, wherein we can estimate a consequential increase in their number to assess any alignment with newly found Type Ia SNe in the ZTF Bright Transient Survey, given their improved spectra data. So our figure of 31,679 GCs in the project could become 2 million considering the improvements outlined above. Therefore, at the figure of 63 times the mass we would expect the LSST to observe a Type Ia SN in

$3\frac{1}{4}$ years, but even at an estimate of 50 times the GC mass, the time necessary to observe an explosion would be 4 years.

Chapter 6

CONCLUSIONS

The project used catalogue data of Type Ia SNe records and images from the ZTF survey, galaxy data and images from HyperLEDA and PanSTARRS with further, deeper images where available from the HST archive.

The 307 Type Ia SNe provided no evidence of a supernova within a globular cluster, so a lower volumetric rate based on the data available was found to be 1.47×10^{-5} yr^{-1} Mpc^{-1} with a lower mass based rate of 4.58×10^{-14} yr^{-1} M$_{\odot}{}^{-1}$.

An upper limit based on mass was estimated, should one Type Ia SN have been observed in one of the 31.679 globular clusters visible to this survey, as 2.52×10^{-12} yr^{-1} M$_{\odot}{}^{-1}$.

The above figures were compared to literature, where it was found that they came closer to the more recent papers and references therein than the earlier items with lower sample sizes (Scannapieco & Bildsten, 2005; Strigari, 2006; Panagia et al., 2007; Ruiter et al., 2009; Maoz et al., 2014; Friedmann & Maoz, 2018; Brown et al., 2019; Frohmaier et al., 2019; Desai et al., 2024).

Further studies searching for these events will be welcomed, especially with the availability of using the LSST with its much improved magnitude limits along with the larger dataset of Type Ia SNe from the ZTF Bright Survey. As mentioned in this report, the improved figures may provide a multiple of 63 times the mass of objects to be scrutinised. Based on this study, the LSST would be expected to observe a Type Ia SN within a GC in around 4 years if the SN rate in GCs is the same as for field stars.

Three Type Ia SN were however found to be potentially associated with objects of interest and may provide evidence of SNe explosions in larger compact stellar systems (massive GCs, UCDs or cEs). Further work is required to discover the exact nature of the objects found, to provide a potential sighting of such events.

Bibliography

Arnett, W. D. & Fu, A. 1989, ApJ, 340, 396

Bahramian, A., Heinke, C. O., Sivakoff, G. R., & Gladstone, J. C. 2013, ApJ, 766, 136

Baron, E., Cooperstein, J., Kahana, S., & Nomoto, K. 1987, ApJ, 320, 304

Baumgardt, H. 2017, MNRAS, 464, 2174

Beasley, M. A. 2020, in Reviews in Frontiers of Modern Astrophysics; From Space Debris to Cosmology (Berlin, Heidelberg: Springer International Publishing), 245–277

Bekki, K., Couch, W. J., Drinkwater, M. J., & Shioya, Y. 2003, MNRAS, 344, 399

Bellm, E. & Kulkarni, S. 2017, Nature Astronomy, 1, 0071

Bellm, E. C., Kulkarni, S. R., Graham, M. J., et al. 2019, PASP, 131, 018002

Branch, D. & Wheeler, J. C. 2017, Type Ic Supernovae (Berlin, Heidelberg: Springer), 379–412

Brown, J. S., Stanek, K. Z., Holoien, T. W. S., et al. 2019, MNRAS, 484, 3785

Canal, R. & Gutiérrez, J. 1997, in Astrophysics and Space Science Library, Vol. 214, White Dwarfs, ed. J. Isern, M. Hernanz, & E. Garcia-Berro, 49

Canal, R., Ruiz-Lapuente, P., & Burkert, A. 1996, ApJL, 456, L101

Chambers, K. C., Magnier, E. A., Metcalfe, N., et al. 2016, arXiv e-prints, arXiv:1612.05560

Da Costa, G. S. & Marino, A. F. 2011, PASA, 28, 28

da Silva, L. A. L. 1993, Ap&SS, 202, 215

Davis, T. M., Hui, L., Frieman, J. A., et al. 2011, ApJ, 741, 67

Deeley, S., Drinkwater, M. J., Sweet, S. M., et al. 2023, MNRAS, 525, 1192

Dekany, R., Smith, R. M., Riddle, R., et al. 2020, PASP, 132, 038001

Dereli, H. 2015, arXiv e-prints, arXiv:1503.04580

Desai, D. D., Kochanek, C. S., Shappee, B. J., et al. 2024, MNRAS, 530, 5016

Doggett, J. B. & Branch, D. 1985, AJ, 90, 2303

Elmegreen, B. G. 1999, Ap&SS, 269, 469

Ferré-Mateu, A., Forbes, D. A., Romanowsky, A. J., Janz, J., & Dixon, C. 2018, MNRAS, 473, 1819

Filippenko, A. V. 1997, ARA&A, 35, 309

Finkbeiner, D. P., Schlafly, E. F., Schlegel, D. J., et al. 2016, ApJ, 822, 66

Fishbach, M. & Fragione, G. 2023, MNRAS, 522, 5546

Foley, R. J., Challis, P. J., Chornock, R., et al. 2013, ApJ, 767, 57

Fregeau, J. M., Gürkan, M. A., Joshi, K. J., & Rasio, F. A. 2003, ApJ, 593, 772

Freire, P. C. C. 2013, in Neutron Stars and Pulsars: Challenges and Opportunities after 80 years, ed. J. van Leeuwen, Vol. 291, 243–250

Fremling, C., Miller, A. A., Sharma, Y., et al. 2020, ApJ, 895, 32

Friedmann, M. & Maoz, D. 2018, MNRAS, 479, 3563

Frohmaier, C., Sullivan, M., Nugent, P. E., et al. 2019, MNRAS, 486, 2308

Fryer, C. L. 1999, ApJ, 522, 413

Fryer, C. L. 2003, Classical and Quantum Gravity, 20, S73

Fryer, C. L. & New, K. C. B. 2003, Living Reviews in Relativity, 6, 2

Fryer, C. L. & New, K. C. B. 2011, Living Reviews in Relativity, 14, 1

Gamezo, V. N., Khokhlov, A. M., Oran, E. S., Chtchelkanova, A. Y., & Rosenberg, R. O. 2003, Science, 299, 77

Garani, R., RAJ, N., & Reynoso-Cordova, J. 2023, JCAP, 2023, 038

Giesers, B., Kamann, S., Dreizler, S., et al. 2019, A&A, 632, A3

Graham, A. W., Driver, S. P., Petrosian, V., et al. 2005, AJ, 130, 1535

Gratton, R., Bragaglia, A., Carretta, E., et al. 2019, A&AR, 27, 8

Guillochon, J., Parrent, J., Kelley, L. Z., & Margutti, R. 2017, ApJ, 835, 64

Harris, W. E. & van den Bergh, S. 1981, AJ, 86, 1627

Heger, A., Fryer, C. L., Woosley, S. E., Langer, N., & Hartmann, D. H. 2003, ApJ, 591, 288

Hénault-Brunet, V., Gieles, M., Sollima, A., et al. 2019, MNRAS, 483, 1400

Hernandez, F., Beckett, G., Clark, P., et al. 2023, arXiv e-prints, arXiv:2311.13981

Hillebrandt, W. & Niemeyer, J. C. 2000, ARA&A, 38, 191

Hillier, D. J. & Dessart, L. 2019, A&A, 631, A8

Ivanova, N., Justham, S., Chen, X., et al. 2013, A&AR, 21, 59

Ivezić, Ž., Kahn, S. M., Tyson, J. A., et al. 2019, ApJ, 873, 111

Izzard, R. G., Hall, P. D., Tauris, T. M., & Tout, C. A. 2012, IAU Symposium, 283, 95

Jha, S. W. 2017, in Handbook of Supernovae, ed. A. W. Alsabti & P. Murdin (Cham, Switzerland: Springer International Publishing), 375

Ji, J. & Bregman, J. N. 2015, ApJ, 807, 32

Jordán, A., Côté, P., Ferrarese, L., et al. 2004, ApJ, 613, 279

Jordán, A., McLaughlin, D. E., Côté, P., et al. 2007, ApJS, 171, 101

Kaiser, N. 1987, MNRAS, 227, 1

Karachentsev, I. D. & Telikova, K. N. 2018, Astronomische Nachrichten, 339, 615

Khokhlov, A., Mueller, E., & Hoeflich, P. 1993, A&A, 270, 223

Lee, J.-W., Kang, Y.-W., Lee, J., & Lee, Y.-W. 2009, Nat, 462, 480

Leonard, P. J. T. 1989, AJ, 98, 217

Li, J., Onken, C. A., Wolf, C., et al. 2022, MNRAS, 515, 3370

Licquia, T. C. & Newman, J. A. 2015, ApJ, 806, 96

Lieb, E. H. & Yau, H.-T. 1987, ApJ, 323, 140

LSST Science Collaboration, Abell, P. A., Allison, J., et al. 2009, arXiv e-prints, arXiv:0912.0201

Maoz, D., Mannucci, F., & Nelemans, G. 2014, ARA&A, 52, 107

Maraston, C. 2005, MNRAS, 362, 799

Maraston, C. & Thomas, D. 2000, ApJ, 541, 126

Marx, S. & Pfau, W. 1992, Astrophotography with the Schmidt Telescope (Cambridge, UK: Cambridge University Press)

Mazzali, P. A., Röpke, F. K., Benetti, S., & Hillebrandt, W. 2007, Science, 315, 825

Meiron, Y. & Kocsis, B. 2019, ApJ, 878, 138

Nagy, A. P., Ordasi, A., Vinkó, J., & Wheeler, J. C. 2014, A&A, 571, A77

NASA/WMAP Science Team. 2014, wmap.gsfc.nasa.gov/universe/uni matter.html, Web based. Accessed 20/02/24

Nomoto, K. 1982, ApJ, 257, 780

Nomoto, K. & Leung, S.-C. 2018, SSR, 214, 67

Nordin, J., Brinnel, V., van Santen, J., et al. 2019, A&A, 631, A147

Norris, M. A. & Kannappan, S. J. 2011, MNRAS, 414, 739

Norris, M. A., Kannappan, S. J., Forbes, D. A., et al. 2014, MNRAS, 443, 1151

Norris, M. A., van de Ven, G., Kannappan, S. J., Schinnerer, E., & Leaman, R. 2019, MNRAS, 488, 5400

Odderskov, I. & Hannestad, S. 2017, JCAP, 2017, 060

O'Leary, R. M., Stahler, S. W., & Ma, C.-P. 2014, MNRAS, 444, 80

Paczynski, B. 1976, in Structure and Evolution of Close Binary Systems, ed. P. Eggleton, S. Mitton, & J. Whelan, Vol. 73, 75

Pagel, B. E. J. 1997, Nucleosynthesis and Chemical Evolution of Galaxies (Cambridge, UK: Cambridge University Press)

Panagia, N., Della Valle, M., & Mannucci, F. 2007, in American Institute of Physics Conference Series, Vol. 924, The Multicolored Landscape of Compact Objects and Their Explosive Origins, ed. T. di Salvo, G. L. Israel, L. Piersant, L. Burderi, G. Matt, A. Tornambe, & M. T. Menna, 373–382

Patat, F., Barbon, R., Cappellaro, E., & Turatto, M. 1994, A&A, 282, 731

Peng, E. W., Jordán, A., Côté, P., et al. 2008, ApJ, 681, 197

Perley, D. A., Fremling, C., Sollerman, J., et al. 2020, ApJ, 904, 35

Perlmutter, S., Aldering, G., Goldhaber, G., et al. 1999, ApJ, 517, 565

Perlmutter, S. & Schmidt, B. P. 2003, in Supernovae and Gamma-Ray Bursters, ed. K. Weiler, Vol. 598 (Berlin, Heidelberg: Springer), 195–217

Pfahl, E., Scannapieco, E., & Bildsten, L. 2009, ApJL, 695, L111

Podsiadlowski, P., Rappaport, S., & Pfahl, E. D. 2002, ApJ, 565, 1107

Pooley, D. 2010, Proceedings of the National Academy of Science, 107, 7164

Pooley, D. 2016, MemSAI, 87, 547

Reynoso-Cordova, J., Regis, M., & Taoso, M. 2022, JCAP, 2022, 038

Richtler, T. 2003, in Stellar Candles for the Extragalactic Distance Scale, ed. D. Alloin & W. Gieren, Vol. 635 (Berlin, Heidelberg: Springer Science and Business Media), 281–305

Riess, A. G., Filippenko, A. V., Challis, P., et al. 1998, AJ, 116, 1009

Röpke, F. K. & Hillebrandt, W. 2004, A&A, 420, L1

Ruiter, A. J., Belczynski, K., & Fryer, C. 2009, ApJ, 699, 2026

Sandage, A. R. 1953, AJ, 58, 61

Sawyer Hogg, H. 1965, PASP, 77, 336

Scannapieco, E. & Bildsten, L. 2005, ApJL, 629, L85

Schwab, J., Quataert, E., & Kasen, D. 2016, MNRAS, 463, 3461

Seth, A. C., van den Bosch, R., Mieske, S., et al. 2014, Nat, 513, 398

Shen, S., Mo, H. J., White, S. D. M., et al. 2003, MNRAS, 343, 978

Smith, R. M., Dekany, R. G., Bebek, C., et al. 2014, in Society of Photo-Optical Instrumentation Engineers (SPIE) Conference Series, Vol. 9147, Ground-based and Airborne Instrumentation for Astronomy V, ed. S. K. Ramsay, I. S. McLean, & H. Takami, 914779

Soker, N. 2011, arXiv e-prints, arXiv:1109.4652

Spitzer, Lyman, J. & Hart, M. H. 1971, ApJ, 164, 399

Starrfield, S., Iliadis, C., & Hix, W. R. 2016, PASP, 128, 051001

Strigari, L. E. 2006, NAR, 50, 566

Taillet, R., Longaretti, P.-Y., & Salati, P. 1995, Astroparticle Physics, 4, 87

Tamura, N., Sharples, R. M., Arimoto, N., et al. 2009, in Globular Clusters - Guides to Galaxies, ed. T. Richtler & S. Larsen (Berlin, Heidelberg: Springer International Publishing), 287

Tauris, T. M. & van den Heuvel, E. P. J. 2006, in Compact stellar X-ray sources, Vol. 39 (Cambridge, UK: Cambridge University Press), 623–665

Tauris, T. M., van den Heuvel, E. P. J., & Savonije, G. J. 2000, ApJL, 530, L93

Thomas, P. A., Drinkwater, M. J., & Evstigneeva, E. 2008, MNRAS, 389, 102

Vitral, E. & Mamon, G. A. 2021, A&A, 646, A63

Voss, R. & Nelemans, G. 2012, A&A, 539, A77

Walder, R., Folini, D., Favre, J. M., & Shore, S. N. 2010, in Astronomical Society of the Pacific Conference Series, Vol. 429, Numerical Modeling of Space Plasma Flows, Astronum-2009, ed. N. V. Pogorelov, E. Audit, & G. P. Zank, 173

Warner, B. 2003, Cataclysmic Variable Stars (Cambridge, UK: Cambridge University Press)

Wheeler, J. C., Höflich, P., Harkness, R. P., & Spyromilio, J. 1998, ApJ, 496, 908

Willmer, C. N. A. 2018, ApJS, 236, 47

Woosley, S. E., Pinto, P. A., Martin, P. G., & Weaver, T. A. 1987, ApJ, 318, 664

Yuan, H., Liu, X., Xiang, M., et al. 2015, ApJ, 799, 135

Zhang, S., Cai, Z., Xu, D., et al. 2023, Science, 380, 494

Zhou, W.-H., Wang, B., Meng, X.-C., Liu, D.-D., & Zhao, G. 2015, Research in Astronomy and Astrophysics, 15, 1701

Ziliotto, T., Milone, A., Marino, A. F., et al. 2023, ApJ, 953, 62